BeBeC-2020-S07


# ASSESSMENT AND COMPARISON OF THE PERFORMANCE OF FUNCTIONAL PROJECTION BEAMFORMING FOR AEROACOUSTIC MEASUREMENTS

Roberto Merino-Martínez[1], Gert Herold[2], Mirjam Snellen[1] and Robert P. Dougherty[3]

[1]Faculty of Aerospace Engineering, Delft University of Technology.
Kluyverweg 1, 2629 HS Delft, The Netherlands.

[2]FG Technische Akustik, TU Berlin.
Einsteinufer 25, 10587 Berlin, Germany.

[3]OptiNav, Inc.
1414 127th NE # 106, Bellevue, Washington, USA 98005.

**Abstract**

Functional Projection Beamforming (FPB) is a method proposed by Dougherty in 2019, based on functional beamforming. It yields the integrated sound spectrum for a given region of integration (ROI) within the functional beamforming source map. FPB does not suffer from the loss of level that can affect functional beamforming, especially for coarse scan grids, high frequencies and high values of the exponent parameter $\nu$. This paper investigates the application of FPB to three different experimental cases: (1) a single speaker emitting broadband noise with a low signal to noise ratio, (2) two closely–placed speakers emitting two incoherent broadband noise signals, and (3) trailing–edge noise measurements of a tripped NACA 0018 airfoil. All measurements were performed with a 64–microphone array in the anechoic open–jet wind tunnel of Delft University of Technology. The performance of FPB is assessed in terms of the accuracy of the frequency spectra obtained and compared with several other well–known acoustic imaging methods. Overall, FPB shows satisfactory results for the three cases investigated, especially for distributed sources, such as trailing–edge noise.

## 1 INTRODUCTION

Noise emissions are becoming increasingly important in many industrial applications and are even a design driver in numerous products. This is especially relevant for the aeronautic and

wind energy sectors, where strict noise regulations limit their expansion and operations [1–3]. In order to reduce noise levels efficiently, it is essential to first determine the locations and relative contributions of all noise sources within this type of complex systems, such as aircraft [4, 5], wind turbines [6, 7] or rotating machinery [8–11]. Phased microphone arrays have become one of the main measurement tools for studying aeroacoustic noise sources [12] in wind–tunnel experiments [13, 14] and field tests [15, 16]. These devices, in combination with acoustic imaging algorithms [17, 18], allow for the estimation of the location and strength of sound sources [19].

Measurements with microphone arrays also reduce the effects of background noise present in the experiment and provide a higher signal to noise ratio (SNR) than measurements with a single microphone. These qualities are especially beneficial for aeroacoustic experiments in closed–section wind tunnels in which the object of study is a relatively quiet sound source, such as an airfoil [20], because the turbulent–boundary–layer noise of the wind–tunnel wall is typically louder than the signal to be measured [21]. However, the use of microphone arrays poses a series of challenges, such as the presence of spurious sources of sidelobes and poor spatial resolution for low frequencies. These challenges are mostly due to the limited number of microphones and limited array size available, which are constrained by budget or practical requirements [18]. In case distributed sound sources, such as trailing–edge noise [22, 23], are the object of study, obtaining accurate estimates of the sound spectrum emitted by the distributed source is also a challenge [24]. Moreover, coherent sound sources are typically not properly solved by conventional acoustic imaging methods [25].

To solve these and other issues, a long list of acoustic imaging methods has been developed in literature [12, 18, 26], each of them tailored for specific applications or noise sources and with different qualities and disadvantages. Previous microphone array benchmark exercises featuring simulated [27, 28] and experimental [29–31] data proved that different imaging methods applied to the same recording data provided considerably different results. Sarradj et al. [32] concluded, after an extensive investigation with synthetic data, that the best method also depends on the frequency of interest.

Functional Projection Beamforming (FPB) is a promising new method that was recently proposed by Dougherty in 2019 [33]. It is based on the functional beamforming method [34–37] and it could be considered as an integration method that yields the sound spectrum for a selected region of integration (ROI) within the functional beamforming source map. Reference [33], where FPB was first introduced, showed successful results obtained by this method when applied to synthetic data and a simple laboratory experiment featuring a string trimmer, compared to other acoustic imaging methods.

The current study discusses the performance of FPB when applied to a more extensive experimental data set[1], consisting of three cases: (1) a single speaker emitting broadband noise with a very low signal to noise ratio, (2) two closely–placed speakers emitting two incoherent broadband noise signals, and (3) trailing–edge noise measurements of a tripped NACA 0018 airfoil. All measurements were performed with a 64–microphone array in the anechoic open–jet wind tunnel of Delft University of Technology (TU Delft). The obtained results by FPB are compared in terms of accuracy of the spectra with other well–known acoustic imaging methods, such as: conventional beamforming [38], functional beamforming [34–37], CLEAN-SC [39] and its enhanced high-resolution version EHR-CLEAN-SC [40], generalized inverse beamforming [41],

[1]This data set is a subset of the cases presented in reference [30].

orthogonal beamforming [42], Covariance Matrix Fitting (CMF) [43], and global optimization (GO) methods [44].

## 2 ACOUSTIC IMAGING METHODS

This section provides a very short description of the acoustic imaging methods employed in this study. For a more detailed explanation, the reader is referred to [12, 18].

### 2.1 Conventional Frequency Domain Beamforming (CFDBF)

Conventional frequency domain beamforming beamforming (CFDBF) [38, 45] is a very popular method, since it is robust, fast and intuitive. However, it is restricted by the Rayleigh resolution limit [46], i.e., the minimum distance at which two sound sources can be distinguished, and it is subject to high sidelobe levels, especially at high frequencies. This technique considers the Fourier transforms of the recorded pressures in each of the $N$ microphones of the array as an $N$–dimensional vector $\boldsymbol{p}(f) \in \mathbb{C}^{N\times 1}$, with frequency $(f)$ dependence

$$\boldsymbol{p}(f) = \begin{pmatrix} p_1(f) \\ \vdots \\ p_N(f) \end{pmatrix}. \tag{1}$$

If we consider a single sound source at the scan point $\boldsymbol{\xi}_j$, the received signal is modeled as $s_j \boldsymbol{g}_j$, where $s_j$ is the source strength and $\boldsymbol{g}_j \in \mathbb{C}^{N\times 1}$ is the so–called steering vector. The steering vector has $N$ components, $g_{j,n}, n \in [1 \cdots N]$, which are the modeled pressure amplitudes at the microphone locations for a sound source with unit strength at that grid point [14]. There are several steering vector formulations available in the literature [47], each of them with different qualities and limitations. For simplicity, omnidirectional monopole sources are normally considered. For a stationary point source, the steering vector is the free–field Green's function of the Helmholtz equation

$$g_{j,n} = \frac{\exp\left(-2\pi i f \Delta t_{j,n}\right)}{4\pi \left\|\boldsymbol{x}_n - \boldsymbol{\xi}_j\right\|} = \frac{\exp\left(\frac{-2\pi i f \left\|\boldsymbol{x}_n - \boldsymbol{\xi}_j\right\|}{c}\right)}{4\pi \left\|\boldsymbol{x}_n - \boldsymbol{\xi}_j\right\|}, \tag{2}$$

where $\|\cdot\|$ is the Euclidean norm of the vector, $i^2 = -1$, $\Delta t_{j,n}$ is the time delay between the emission and the reception of the signal by the observer and $\boldsymbol{x}_n = (x_n, y_n, z_n) \in \mathbb{R}^{N\times 3}, n = 1 \ldots N$ are the locations of the $N$ microphones.

An estimate for the source autopower, $A$, at a source located at grid point $\boldsymbol{\xi}_j$ is obtained by minimizing (in a least–squares sense) the difference between the recorded pressure vector, $\boldsymbol{p}$, and the modeled pressures for a source at that grid point $\boldsymbol{\xi}_j$, $s_j \boldsymbol{g}_j$

$$A\left(\boldsymbol{\xi}_j\right) = \frac{\boldsymbol{g}_j^* \left\langle \boldsymbol{p}\boldsymbol{p}^* \right\rangle \boldsymbol{g}_j}{\left\|\boldsymbol{g}_j\right\|^4} = \boldsymbol{w}_j^* \boldsymbol{C} \boldsymbol{w}_j. \tag{3}$$

In Eq. (3), an asterisk, $(\cdot)^*$, denotes the complex conjugate transpose, $\left\langle \cdot \right\rangle$ denotes the time

average of several snapshots and $\boldsymbol{w}_j$ is the weighted steering vector (once again, several different formulations for the weighted steering vector exist in literature [47]):

$$\boldsymbol{w}_j = \frac{\boldsymbol{g}_j}{\boldsymbol{g}_j^* \boldsymbol{g}_j} = \frac{\boldsymbol{g}_j}{\left\|\boldsymbol{g}_j\right\|^2}, \tag{4}$$

and $\boldsymbol{C}$ is the $N \times N$ cross–spectral matrix (CSM) of the measured pressures, generated by averaging the Fourier–transformed sample blocks over time

$$\boldsymbol{C} = \left\langle \boldsymbol{p}\boldsymbol{p}^* \right\rangle. \tag{5}$$

A CFDBF source map can be constructed by applying Eq. (3) to the $J$ points defining the selected scan grid. Assuming that the sound sources are mutually incoherent, such source map is the summation of the point spread functions (PSFs) of the actual sound sources. Since the strengths of the sources are always positive because $\boldsymbol{C}$ is Hermitian and positive semidefinite, (and due to the fact that noise is present in practice), the terms in the sum are non–negative, and, thus, the source map represents an overestimation of the actual source levels when multiple sound sources are present.

Considering the presence of unwanted noise in the array measurements and assuming deterministic steering vectors [33], the recorded pressures in Eq. (1) can be rewritten as

$$\boldsymbol{p} = \boldsymbol{G}\boldsymbol{s} + \boldsymbol{n}, \tag{6}$$

where $\boldsymbol{G} \in \mathbb{C}^{N \times J}$ is a matrix containing the steering vectors $\boldsymbol{g}_j$ of each grid point in its columns $[\boldsymbol{g}_1 \ldots \boldsymbol{g}_J]$ and $\boldsymbol{s}$ the $J \times 1$ vector containing the actual source amplitudes of each grid point $[s_1 \ldots s_J]^\mathsf{T}$. Here $(\cdot)^\mathsf{T}$ represents the transpose. The $N \times 1$ vector $\boldsymbol{n}$ represents the unwanted noise that the array receives, such as background noise, or signals from sources outside of the scan grid.

Meanwhile, the CSM from Eq. (5) can be expressed using Eq. (6) as

$$\boldsymbol{C} = \left\langle (\boldsymbol{G}\boldsymbol{s} + \boldsymbol{n})(\boldsymbol{G}\boldsymbol{s} + \boldsymbol{n})^* \right\rangle \approx \boldsymbol{G}\boldsymbol{S}\boldsymbol{G}^* + \boldsymbol{N}, \tag{7}$$

where $\boldsymbol{S}$ is the source cross–spectral matrix $\boldsymbol{S} = \left\langle \boldsymbol{s}\boldsymbol{s}^* \right\rangle$, and $\boldsymbol{N}$ cross–spectral matrix due to the unwanted noise. If all the sound sources present are mutually incoherent, $\boldsymbol{S}$ is a diagonal matrix.

Some integration methods have been proposed in the literature, such as the Source Power Integration (SPI) and its variants [14, 48–50], which reduce the influence of the array's PSF when studying the sound levels of distributed sources within a ROI. These methods have been applied to a benchmark with simulated data [27] and to wind–tunnel experiments featuring airframe noise sources [23, 51, 52] with successful results. Thus, this approach is also employed in this study.

### 2.2 Functional Beamforming (FUNBF)

Functional beamforming (FUNBF) is a method developed by Dougherty [34, 35] which is a modification of the CFDBF algorithm. Since the CSM is Hermitian and positive semidefinite,

it can be expressed as its eigenvalue decomposition

$$\boldsymbol{C} = \boldsymbol{U}\boldsymbol{\Sigma}\boldsymbol{U}^* = \sum_{n=1}^{N} \sigma_n \boldsymbol{u}_n \boldsymbol{u}_n^*, \tag{8}$$

where $\boldsymbol{U}$ is a unitary matrix whose columns are the eigenvectors $(\boldsymbol{u}_1, \ldots, \boldsymbol{u}_N)$ of $\boldsymbol{C}$, and $\boldsymbol{\Sigma}$ is a diagonal matrix whose diagonal elements are the real–valued eigenvalues $(\sigma_1, \ldots, \sigma_N)$ of $\boldsymbol{C}$. It should be noted that $\boldsymbol{\Sigma}^*\boldsymbol{\Sigma} = \boldsymbol{I}$, where $\boldsymbol{I}$ is an $N \times N$ identity matrix.

The source autopower expression for the functional beamformer is

$$A_\nu(\boldsymbol{\xi}) = \left[\boldsymbol{w}^* \boldsymbol{C}^{\frac{1}{\nu}} \boldsymbol{w}\right]^\nu = \left[\boldsymbol{w}^* \boldsymbol{U}\boldsymbol{\Sigma}^{\frac{1}{\nu}} \boldsymbol{U}^* \boldsymbol{w}\right]^\nu, \tag{9}$$

with $\nu \geq 1$ a parameter which needs to be set by the user. It can be easily proven that for the case of $\nu = 1$ the CFDBF method is obtained.

For single sound sources, the PSF, which has a value of one at the correct source locations and alias points and a value less than one elsewhere, is powered to the exponent $\nu$. Therefore, powering the PSF at a sidelobe will lower its level, leaving the true source value virtually identical [34] if an adequate grid is used [36]. For ideal conditions, the dynamic range of functional beamforming should increase linearly with the exponent value, $\nu$. On the other hand, a large value of $\nu$ can cause a decay in the sound levels measured in practice, due to the sensitivity of this method to a mismatch in the steering vector, which occurs when a coarse grid is employed [34, 36, 37, 53] and the positions of the grid points do not coincide exactly with the source locations. This is an increasingly important source of errors for high frequencies or high values of the exponent $\nu$, but it can be solved by employing a finer grid [30]. For this study it was decided to use $\nu = 8$ after performing a sensitivity analysis.

The computational time for the functional beamforming is basically identical to the CFDBF one, since the only relevant operation added is the eigenvalue decomposition of $\boldsymbol{C}$.

In previous work, functional beamforming has been applied to numerical simulations [34–36], controlled experiments with components in a laboratory [34, 35] and to full–scale aircraft flyover measurements under operational conditions [20, 36, 37, 54]. A similar integration method as the SPI technique was used for isolating and quantifying noise sources in flyover measurements [20, 52, 55] and is also used in this paper.

### 2.3 Projection Beamforming (PB)

Projection Beamforming (PB) [33] is an integration method that measures the sound spectra generated over a selected ROI. It characterizes the ROI as a subspace in the array steering vector space, projecting the array's CSM onto this subspace and taking the average of the diagonal elements of the outcome.

This technique begins with the singular value decomposition of the matrix $\boldsymbol{G} \in \mathbb{C}^{N \times J}$ (which contains the steering vectors $\boldsymbol{g}_j$ of each grid point)

$$\boldsymbol{G} = \tilde{\boldsymbol{U}}\tilde{\boldsymbol{\Sigma}}\tilde{\boldsymbol{V}}^* \approx \tilde{\boldsymbol{U}}_1 \tilde{\boldsymbol{\Sigma}}_{11} \tilde{\boldsymbol{V}}_1^*, \tag{10}$$

where $\tilde{\boldsymbol{U}}$ and $\tilde{\boldsymbol{V}}$ contain the left and right singular vectors of $\boldsymbol{G}$ ($\tilde{u}_n$ and $\tilde{v}_n$), respectively, and $\tilde{\boldsymbol{\Sigma}}$ contains the singular values $\tilde{\sigma}_n$. The approximation on the right hand side of Eq. (10) considers

the $m$ leading, significant singular values of $\boldsymbol{G}$, such that $\tilde{\boldsymbol{\Sigma}}_{11}$ is an $m \times m$ submatrix of $\tilde{\boldsymbol{\Sigma}}$, and $\tilde{\boldsymbol{U}}_1$ and $\tilde{\boldsymbol{V}}_1$ are the first $m$ columns of $\tilde{\boldsymbol{U}}$ and $\tilde{\boldsymbol{V}}$, respectively. By definition $m \leq \min(N,J)$. A suggestion for selecting the value of $m$ is given at the end of this section.

Substituting Eq. (10) into Eq. (7) provides

$$\boldsymbol{C} \approx \tilde{\boldsymbol{U}}_1 \tilde{\boldsymbol{\Sigma}}_{11} \tilde{\boldsymbol{V}}_1^* \boldsymbol{S} \tilde{\boldsymbol{V}}_1 \tilde{\boldsymbol{\Sigma}}_{11} \tilde{\boldsymbol{U}}_1^* + \boldsymbol{N} = \tilde{\boldsymbol{U}}_1 \boldsymbol{W} \tilde{\boldsymbol{U}}_1^* + \boldsymbol{N}, \tag{11}$$

where $\boldsymbol{W}$ is an $m \times m$ source strength matrix $\boldsymbol{W} = \tilde{\boldsymbol{\Sigma}}_{11} \tilde{\boldsymbol{V}}_1^* \boldsymbol{S} \tilde{\boldsymbol{V}}_1 \tilde{\boldsymbol{\Sigma}}_{11}$.

Using the fact that the columns of $\tilde{\boldsymbol{U}}_1$ are orthonormal, the Frobenius norm of $\left\| \boldsymbol{C} - \tilde{\boldsymbol{U}}_1 \boldsymbol{W} \tilde{\boldsymbol{U}}_1^* \right\|_{\mathrm{F}}$ is minimized using a linear least–squares fit as

$$\boldsymbol{W} \approx \tilde{\boldsymbol{U}}_1^* \boldsymbol{C} \tilde{\boldsymbol{U}}_1, \tag{12}$$

Therefore, the portion of the CSM associated with $\boldsymbol{W}$, i.e., the part of $\boldsymbol{C}$ due to the actual sound sources can be rewritten as

$$\tilde{\boldsymbol{U}}_1 \boldsymbol{W} \tilde{\boldsymbol{U}}_1^* \approx \tilde{\boldsymbol{U}}_1 \tilde{\boldsymbol{U}}_1^* \boldsymbol{C} \tilde{\boldsymbol{U}}_1 \tilde{\boldsymbol{U}}_1^* = \boldsymbol{R}\boldsymbol{C}\boldsymbol{R}, \tag{13}$$

where $\boldsymbol{R} = \tilde{\boldsymbol{U}}_1 \tilde{\boldsymbol{U}}_1^*$ is the projection matrix onto the subspace defined by the ROI. Thus, $\boldsymbol{R}\boldsymbol{C}\boldsymbol{R}$ represents the projection of $\boldsymbol{C}$ onto the ROI's subspace. The autopower estimate of PB for a selected ROI is the average of the diagonal elements of $\boldsymbol{R}\boldsymbol{C}\boldsymbol{R}$

$$A_{\mathrm{PB}} = \frac{1}{N} \mathrm{tr}(\boldsymbol{R}\boldsymbol{C}\boldsymbol{R}), \tag{14}$$

where $\mathrm{tr}(\cdot)$ denotes the trace of a matrix.

The only choice left to be made by the user is the ROI and the parameter $m$ determining the amount of singular values of $\boldsymbol{G}$ that are significant. Let the singular values of $\boldsymbol{G}$ be arranged in decreasing order be $\tilde{\sigma}_1, \ldots, \tilde{\sigma}_N$. A relative singular value sum function [33] can be defined as

$$\tilde{s}(i) = \begin{cases} 0 & \text{for } i = 1; \\ \frac{\sum_{j=1}^{i-1} \tilde{\sigma}_j}{\sum_{j=1}^{N} \tilde{\sigma}_j} & \text{for } i = 2, \ldots, N. \end{cases} \tag{15}$$

A sum value of $\tilde{s}(i)$, $\tilde{s}_0$, needs to be defined to express the proportion of significant singular values. A value of $\tilde{s}_0 = 0.999$ was used in this paper, i.e., it represents 99.9% of the energy contained in all the singular values. The index $i_0$ is then defined as the smallest index such that $\tilde{s}(i_0) \geq \tilde{s}_0$. In case that condition is never met, $i_0$ adopts the value of $N$.

The projection matrix can be expressed as its eigenvalue decomposition $\boldsymbol{R} = \boldsymbol{U}_R \boldsymbol{D} \boldsymbol{U}_R^*$, where $\boldsymbol{D}$ is a diagonal matrix whose elements $d_i$ are defined as

$$d_i = \begin{cases} 1 & \text{for } i = 1, \ldots, i_0 - 1; \\ \sqrt{\frac{\tilde{s}_0 - \tilde{s}(i_0 - 1)}{\tilde{s}(i_0) - \tilde{s}(i_0 - 1)}} & \text{for } i = i_0; \\ 0 & \text{for } i = i_0 + 1, \ldots, N. \end{cases} \tag{16}$$

The value of $d_{i_0}$ is defined as intermediate between 0 and 1 as a way to smooth the final spectra.

Since Eq. (14) was derived from a linear least–squares approach, it is limited in terms of

dynamic range.

### 2.4 Functional Projection Beamforming (FPB)

The dynamic range of PB can be considerably improved by combining the PB idea with the non–linear formulation of FUNBF from Eq. (9, see section 2.2). In a similar way as PB was applied to the CFDBF source map, FPB is applied to the source map obtained with FUNBF. Analogously to Eq. (12), an approximation to $\boldsymbol{W}^{\frac{1}{\nu}}$ to minimize $\left\| \boldsymbol{C}^{\frac{1}{\nu}} - \tilde{\boldsymbol{U}}_1 \boldsymbol{W}^{\frac{1}{\nu}} \tilde{\boldsymbol{U}}_1^* \right\|_{\mathrm{F}}$ is

$$\boldsymbol{W}^{\frac{1}{\nu}} \approx \tilde{\boldsymbol{U}}_1^* \boldsymbol{C}^{\frac{1}{\nu}} \tilde{\boldsymbol{U}}_1, \tag{17}$$

and, hence,

$$\boldsymbol{W} \approx \left( \tilde{\boldsymbol{U}}_1^* \boldsymbol{C}^{\frac{1}{\nu}} \tilde{\boldsymbol{U}}_1 \right)^{\nu}, \tag{18}$$

Following the same procedures as for deriving Eq. (14) in PB, the Functional Projection Beamforming (FPB) [33] can be derived as

$$A_{\mathrm{FPB}} = \frac{1}{N} \mathrm{tr} \left[ \left( \boldsymbol{R} \boldsymbol{C}^{\frac{1}{\nu}} \boldsymbol{R} \right) \right)^{\nu} \Bigg], \tag{19}$$

FPB offers a higher dynamic range (determined by the user–defined parameter $\nu$) than PB and, as well as PB, can be applied to coherent source distributions. The resolution of this method, however, is similar to CFDBF [33].

### 2.5 Orthogonal Beamforming (OB)

Orthogonal beamforming (OB) [42, 56, 57], similarly to FUNBF, is also based on the eigenvalue decomposition of the CSM. It builds on the idea of separating the signal and the noise subspace [58]. In a setup with $K$ incoherent sources and $K < N$, it is reasonable to assume that the $(N-K)$ smallest eigenvalues are attributed to noise and are all equal to $\hat{n}^2$. The CSM eigenvalue decomposition can be written as

$$\boldsymbol{C} = \boldsymbol{U}_S \boldsymbol{\Sigma}_S \boldsymbol{U}_S^* + \hat{n}^2 \boldsymbol{I}, \tag{20}$$

where $\hat{n}^2$ contains the power from uncorrelated sound sources (e.g., generated by non–acoustic pressure fluctuations, the microphone electronics and data acquisition hardware). Hence, the eigenvectors in $\boldsymbol{U}_S$ span the signal subspace of $\boldsymbol{U}$, whereas the remaining eigenvectors span the noise subspace.

Similarly to the $N \times J$ matrix $\boldsymbol{G}$ in Eq. (6), let the $N \times K$ matrix $\tilde{\boldsymbol{G}}$ contain the transfer functions (i.e., the steering vectors) between the $K$ sources and $N$ microphones $[\boldsymbol{g}_1 \ldots \boldsymbol{g}_K]$ (see Eq. (2)). As shown in [57], the matrix $\boldsymbol{\Sigma}_S$ is mathematically similar to $(\tilde{\boldsymbol{G}}^* \tilde{\boldsymbol{G}}) \boldsymbol{S}$ and, therefore, has the same eigenvalues. Here $\boldsymbol{S}$ is the CSM of the source signals, as in Eq. (7). The main idea behind orthogonal beamforming is that each eigenvalue of $\boldsymbol{\sigma}_S$ can be used to estimate the absolute source level of one source, from the strongest sound source within the map to the weakest, assuming orthogonality between steering vectors.

In a second step, these sources are mapped to specific locations. This is done by assigning the eigenvalues to the location of the highest peak in a special beamforming sound map, which is purposely constructed from a rank–one CSM that is synthesized only from the corresponding eigenvector. Hence, the map is the output of the spatial beamforming filter for only one single source and the highest peak in this map is an estimate of the source location. The beamforming map can be constructed on the basis of vector–vector products and is, therefore, computationally very fast.

An important parameter in the eigenvalue decomposition, which has to be adjusted by the user, is the number of eigenvalues $k$ that span the signal subspace $\boldsymbol{U}_S$. In a practical measurement, a reliable approach is to estimate the number of incoherent sources $K$ present in the experiment, by observing the number of dominant eigenvalues of $\boldsymbol{C}$ for example, and choose a value $k > K$. In this paper it was selected $k = 20$.

### 2.6 CLEAN–SC

CLEAN–SC [39] is a frequency domain deconvolution technique developed by Sijtsma and based on the radio–astronomy method CLEAN–PSF [59]. Dougherty and Stoker [60] already applied CLEAN–PSF to aeroacoustic measurements for the first time in 1998. CLEAN–SC uses the fact that the sidelobes are spatially coherent with the main lobe [39]. CLEAN–SC starts from the assumption that the CSM can be written as a summation of contributions from $K$ incoherent sources:

$$\boldsymbol{C} = \sum_{k=1}^{K} \left\langle \boldsymbol{p}_k \boldsymbol{p}_k^* \right\rangle. \tag{21}$$

Herein, $\boldsymbol{p}_k$ are the $N$–dimensional acoustic "source vectors" representing the Fourier components of the signals from the $k^{\text{th}}$ source. The assumption of Eq. (21) is valid under the following conditions:

- The CSM is calculated from a large number of time blocks, so that the ensemble averages of the cross–products $\boldsymbol{p}_k \boldsymbol{p}_l^*, k \neq l$, can be neglected.
- There is no decorrelation of signals from the same source between different microphones (e.g., due to sound propagation through turbulence).
- All sound sources present are incoherent.
- There is no additional incoherent noise.

The CLEAN–SC algorithm starts with finding the steering vector yielding the maximum value of the beamforming source map (Eq. (3)), say at scan point $\boldsymbol{\xi}_j$:

$$\max(A) = A\left(\boldsymbol{\xi}_j\right) = \boldsymbol{w}_j^* \boldsymbol{C} \boldsymbol{w}_j. \tag{22}$$

The corresponding "source component" $\boldsymbol{h}_j$ representing the identified source's contribution to the CSM is defined by

$$\boldsymbol{h}_j = \frac{\boldsymbol{C}\boldsymbol{w}_j}{A\left(\boldsymbol{\xi}_j\right)}. \tag{23}$$

Insertion of Eq. (21) yields

$$\boldsymbol{h}_j = \frac{\sum_{k=1}^{K} \left(\boldsymbol{p}_k^* \boldsymbol{w}_j\right) \boldsymbol{p}_k}{A\left(\boldsymbol{\xi}_j\right)}. \tag{24}$$

The source component $\boldsymbol{h}_j$ is entirely based on the measured data and can be considered as an improved version of the steering vector $\boldsymbol{g}_j$ because it is more proportional to the unknown source vector $\boldsymbol{p}_j$. Thus, CLEAN–SC has low sensitivity to errors made in the source model that describe the sound propagation, i.e., if the steering vectors considered do not exactly match with the source vectors [61].

If the sources are well separated, then the term between parentheses in Eq. (24) is large when there is a close match between $\boldsymbol{w}_j$ and the peak source and small for the other sources. Then, the source component provides a good estimate of the strongest source vector, even if this vector is not exactly proportional to the corresponding steering vector.

Thus, we arrive at the following estimate:

$$\boldsymbol{p}_k \boldsymbol{p}_k^* = \frac{\left(A\left(\boldsymbol{\xi}_j\right)\right)^2 \boldsymbol{h}_j \boldsymbol{h}_j^*}{|\boldsymbol{p}_k^* \boldsymbol{w}_j|^2} \approx A\left(\boldsymbol{\xi}_j\right) \boldsymbol{h}_j \boldsymbol{h}_j^*. \tag{25}$$

This expression is subtracted from the CSM and the source is given an amplitude which is related to the average autopower of the microphone array. This quantity is often multiplied by a so–called loop gain or damping factor $\tilde{\varphi}$, with $0 < \tilde{\varphi} \leq 1$ [39]. This is done to take into account the contributions of other sound sources, which are normally small [40]. Hence, the CSM for the $i^{\text{th}}$ iteration of CLEAN–SC is calculated as

$$\boldsymbol{C}^{(i)} = \boldsymbol{C}^{(i-1)} - \tilde{\varphi} A\left(\boldsymbol{\xi}_j\right) \boldsymbol{h}_j \boldsymbol{h}_j^*. \tag{26}$$

Then, the same procedure is repeated for the remaining CSM, until a certain stop criterion is fulfilled [39]. Ideally, the remaining CSM is "empty" after the iteration process. In other words, its norm should be small compared to the one from the original CSM. The new source map is obtained by the summation of the clean beams of the $K$ identified sound sources and the remaining degraded CSM [40].

Recently, an enhanced higher–resolution version of CLEAN–SC (EHR–CLEAN–SC) [40, 61–63] has been proposed, which increases the spatial resolution of the standard CLEAN–SC beyond the Rayleigh resolution limit. This technique achieves super–resolution by relocating the "source marker" from the actual source location to a location on the main lobe where the combined influence of the other $(K-1)$ sound sources is the minimized [61, 62]. To determine the best source marker positions, an iterative procedure starting with the standard CLEAN–SC solution can be performed. This approach is performed for each frequency because the sidelobe level strongly depends on the frequency considered [12]. The number of expected sound sources $K$ has to be selected by the user in as similar way as for OB. In this paper, all the eigenvalues of the CSM below 6 dB of the maximum eigenvalue were considered for the cases with speakers and 5 sources were considered for the airfoil cases [30]. The additional required computation time with respect to the standard version of CLEAN–SC is limited as long as the number of incoherent sound sources $K$ is limited.

The source maps obtained by EHR–CLEAN–SC (and the other CLEAN–SC versions) can be integrated to obtain a sound spectrum by simply adding the powers of the deconvoluted *clean*

sources calculated within a predefined ROI [39].

This method has been applied successfully to simulated data, to experimental data using speakers in an anechoic chamber [40, 61–63] and to open–jet wind–tunnel measurements of a full–scale landing gear [52, 64].

In this paper, results from both CLEAN–SC and EHR–CLEAN–SC are presented for comparison.

### 2.7 Covariance Matrix Fitting (CMF)

The Covariance Matrix Fitting (CMF) method [43, 65, 66] (also called in literature as Spectral Estimation Method (SEM)) is intended for the location of distributed sound sources. It is based on the description of the sound sources by mathematical models that depend on several unknown parameters. It is assumed that the Power Spectral Density (PSD) of the sources can then be expressed in terms of these parameters.

The choice of the source model is based on the fact that an extended sound source may only be viewed as an equivalence class between source functions radiating the same pressure field on a phased microphone array. In many applications, a majority of sound sources have smooth directivity patterns. This means that if the aperture angle of a microphone array seen from the overall source region is not too large, the directivity pattern of each region may be considered as isotropic within this aperture, neglecting its directivity.

Therefore, CMF models the array CSM $C_{m,n}$ with a set of $J$ uncorrelated monopoles with unknown autopowers $\tilde{x}_j$ by minimizing the following cost function (mean least–squares error between the measured and modeled matrices)

$$F(\boldsymbol{s}) = \sum_{m,n=1}^{N} \left| C_{m,n} - \sum_{j=1}^{J} g_{j,m} \tilde{x}_j g_{j,n}^{*} \right|^2 . \tag{27}$$

The constraint of a non–negative PSD is satisfied by defining $\tilde{x}_j$ as the square of the source strength $s_j$, i.e. $\tilde{x} = s^2$. The source strengths values of the $J$ incoherent monopoles are contained in the vector $\boldsymbol{s}$. This variable change allows for the use of efficient optimization methods for solving unconstrained problems. The resulting non–linear minimization problem is solved using an iterative procedure based on a conjugate gradient method algorithm. The solution generally converges fast with only a few hundred iterations.

CMF provides improved spatial resolution and a reduction of the sidelobe level compared to CFDBF. This technique has shown its efficiency in noiseless environments, on numerical simulations [43] and on data measured during experiments performed with an Airbus A320 half–aircraft model in the open–jet anechoic wind tunnel CEPRA 19 at ONERA in France, [43, 67, 68].

### 2.8 Generalized Inverse Beamforming (GIBF)

Generalized inverse beamforming (GIBF) [41, 69] is an inverse method based on the eigenvalue decomposition of the CSM. Unlike direct beamforming methods, in which each potential source is assumed to be uncorrelated, GIBF takes into account the possible source interference by resolving all the sources at once.

This fact allows to resolve both correlated/uncorrelated sources, as well as sparse and spatially–distributed sources. Similarly as in OB, GIBF also requires the user to select the assumed number of eigenvalues to consider. Each eigenvalue represents the overall strength related to a coherent source distribution under the constraint of orthogonality. This method (with different regularization strategies) was recently applied to airfoil–noise [70–72] and counter rotating open rotor [11] measurements in open–jet wind tunnels.

For the integration of the GIBF sound maps, the pressure values of each scanning grid point are summed and then squared due to the assumption of source coherence.

In this paper, the regularization process recently proposed by Zamponi et al. [70, 71] and an NNLS solver [73] were employed and referred to as GIBF and GIBF–NNLS, respectively.

### 2.9 Global optimization methods (GO)

A method was presented by Malgoezar et al. [44] where the search for the locations and amplitudes of sound sources is treated as a global optimization (GO) problem. The search can be easily extended to more unknowns, such as additional geometrical or environmental parameters, and more complex situations with, for example, multiple sound sources or reflections being present. The method is essentially grid–free and can overcome the Rayleigh resolution limit.

The presence of sidelobes will, however, hamper the optimization as they act as local optima against which the global optimum needs to be found. In [44] a variation of the genetic algorithm, called differential evolution, was proposed as a global optimization method. These optimization methods mimic natural evolution by using populations of solutions, where promising solutions are given a high probability to reproduce and worse solutions have a lower probability to reproduce.

The locations of the sources are sought by using a global optimization method, instead of considering a predefined grid of potential source locations. This way, estimates for source positions and source strengths are obtained as a solution of the optimization and do not need to be obtained from a source map. As aforementioned for other methods, the number of sound sources present is not known *a priori*, but a simple iterative process can be performed using as first guess the number of dominant eigenvalues of the CSM.

In order to use global optimization methods, a cost function has to be defined. This can be done by constructing a CSM from a signal model and comparing it to the *measured* CSM. This objective function can then in turn be used in an optimizer, such as differential evolution. By minimizing the objective function over many generations, the solution will converge to the actual position and strength of the sound sources. For this study, the setting parameters required for the GO method [44] were a population size $q$ of 128, a multiplication factor $F$ of 0.6, a crossover probability of $p_C$ of 0.55. A total of 4 runs were performed, each of them with 1000 generations.

The GO method does not provide source maps like the other acoustic imaging methods explained above, but instead energy landscapes for each variable searched (in this case the three coordinates $(x, y, z)$ and the source strength. These are not shown in this paper for brevity reasons, and only the frequency spectra obtained are presented for comparison purposes. The interested reader is referred to [44] for examples of these energy landscapes.

### 2.10 Overview of the contributors and parameters for each method

Table 1 contains a list of the acoustic imaging methods employed for the comparison in this paper, as well as the institution contributing (TU Delft, TU Berlin and the von Karman Institute for Fluid Dynamics (VKI)) and the most important parameters for each method. Some of these results were extracted from [30]. The results provided by TU Berlin were computed using the open source Python package *Acoular* [74].

*Table 1: Overview of the contributors and parameters for each method.*

| Method | Contributor | Parameters |
|---|---|---|
| CFDBF | TU Delft [30] | SPI integration |
| FUNBF | TU Delft [30] | $\nu = 8$, SPI integration |
| FPB | TU Delft | $\nu = 8$ , $\tilde{s}_0 = 0.999$ |
| OB | TU Berlin | $k = 20$ |
| CLEAN–SC | TU Berlin | $\tilde{\varphi} = 0.6$ |
| EHR–CLEAN–SC | TU Delft [30] | $\tilde{\varphi} = 0.99$ (speakers); 0.4 (airfoil) |
| CMF | TU Berlin | NNLS solver |
| GIBF | VKI [30] | $L_1$ norm regularization [70, 71] |
| GIBF–NNLS | TU Berlin | NNLS solver, $k = 20$ |
| GO | TU Delft | $q = 128$, $F = 0.6$, $p_C = 0.55$ |

## 3 EXPERIMENTAL SETUP

The experiments were performed in the anechoic plenum of the vertical open–jet wind tunnel (A–tunnel) at Delft University of Technology [23, 75], which is located in a room covered with wedges made of *Flamex Basic* acoustic absorbing foam [76] that a cut–off frequency of 200 Hz, i.e., free–field propagation conditions apply for higher frequencies. A microphone array consisting of 64 *G.R.A.S.* 40PH analog free–field microphones [77] with integrated constant current power amplifiers was employed for all the experiments.

The microphone distribution employed for the measurements featuring speakers was optimized for a frequency range between 1 kHz and 10 kHz [63], see Fig. 1a. It has a diameter of approximately 2 m. This array is referred to as *Array 1*. In the same plot, the relative position of the two Visaton K 50 SQ speakers [78] used for the experiments can be observed. Both of them were situated at a distance of 1 m from the array plane and have a baffle diameter of approximately 45 mm. The ($x$, $y$, $z$) coordinates of the centers of the speakers (with the $x$ and $y$ axes centered at the array center microphone, see Fig. 1a, and the $z$ axis normal to the array plane pointing towards the speakers) are (-0.05 m, 0.05 m, 1 m) for the left speaker and (0.3 m, 0.05 m, 1 m) for the right one. The test cases featuring speakers were performed without flow in the wind tunnel, i.e., simply using the facility as an anechoic chamber. The point spread function (PSF) [18] of this microphone array (*Array 1*) is shown in Fig. 1b for a simulated point

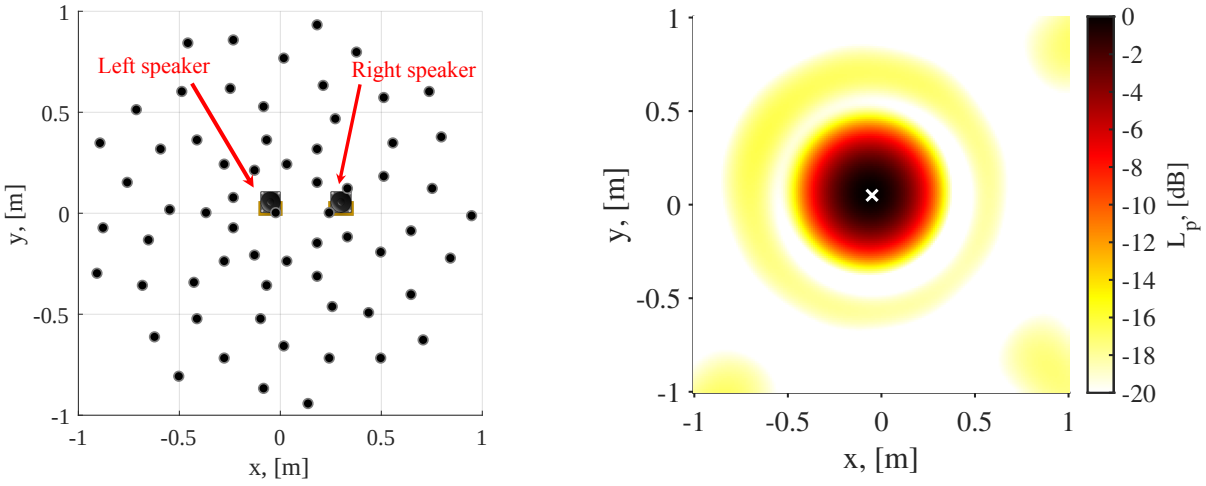


*Figure 1: (a) Microphone distribution of the Array 1 (seen from behind) and relative position of the two speakers (situated 1 m away from the array's plane). (b) PSF of the Array 1 for a point source at the position of the left speaker (denoted by the white × symbol) emitting sound within a one–third–octave band centered at 630 Hz.*

source located at the same position as the left speaker emitting sound within a one–third–octave frequency band centered at 630 Hz.

For each measurement a sampling frequency of 50 kHz and 60 s of recording time were used. The acoustic data were averaged in time blocks of 8192 samples (giving a time block duration of 163.84 ms) and windowed using a Hanning weighting function with 50% data overlap, following Welch's method [79]. One–third–octave frequency bands will be used in the paper for comparison purposes. The frequency range of interest extended from 500 Hz to 5 kHz, which is typically the range considered for similar airfoil noise experiments [23, 80–83].

For each test case, some considerations should be noted:

### 3.1 Case I: Single speaker

For the first test case, only the left speaker (see Fig. 1a) emitted sound. A broadband noise signal was generated synthetically ($SNR_1$ in Fig. 2a). The values shown are sound pressure levels $L_p$ in decibels with a reference pressure of 20 $\mu$Pa. The amplitude of this signal was reduced mathematically so that part of its frequency spectrum (below 1250 Hz) would be below the background noise of the facility, i.e., with a negative SNR. A constant offset of approximately -32 dB was, thus, applied to the $SNR_1$ spectrum to obtain $SNR_2$, which is the object of study for the single speaker case. For the frequency bands below 1250 Hz in the $SNR_2$ case, the sound spectrum is, therefore, calculated by subtracting the aforementioned offset from the $SNR_1$ case.

For all cases, the average signal of all the microphones of the array was considered as the reference signal for comparison with the results of the acoustic imaging methods. The signal of each microphone was corrected for expressing the sound level at one meter from the sound source. For all methods, a scan grid ranging from $x = -1$ m to $x = 1$ m and from $y = -1$ m

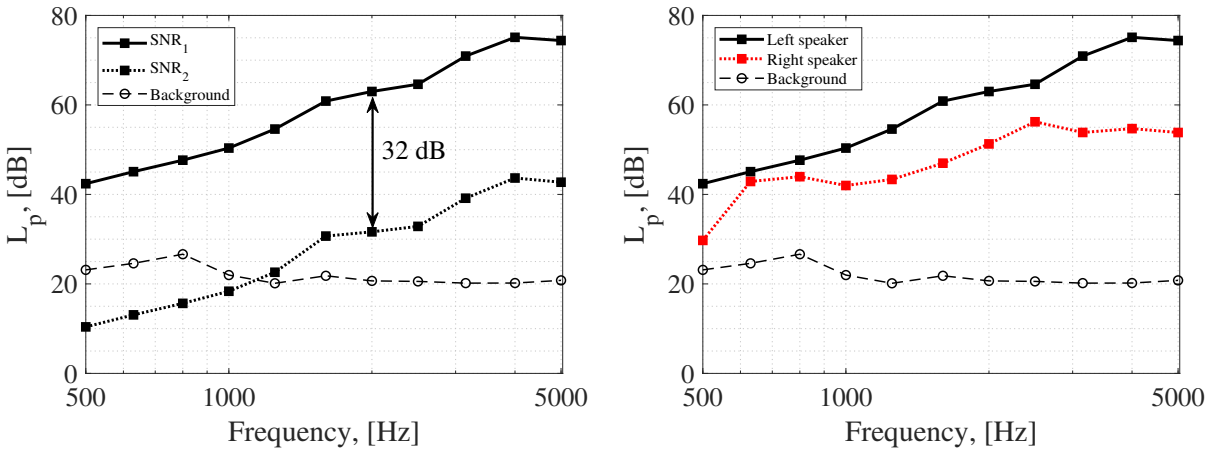


*Figure 2: One–third–octave band frequency spectra recorded by the array (averaged over all microphones) for: (a) The single speaker case for the two SNR cases. (b) The case with two speakers. The background noise spectrum of the facility is also plotted in both graphs for reference.*

to $y = 1$ m was used, with $z = 1$ m and spacing between grid points of $\Delta x = \Delta y = 0.01$ m. The obtained source maps were integrated over a square ROI centered at the left speaker (from $x = -0.15$ m to $x = 0.05$ m and from $y = -0.05$ m to $y = 0.15$ m, with $z = 1$ m), see the dashed squares in Fig. 4.

### 3.2 Case II: Two speakers

For the case with two speakers, both speakers (left and right, see Fig. 1a) emitted sound simultaneously. The same synthetic broadband noise signal as in Case I was played by the left speaker with the volume of the $\mathrm{SNR}_1$ case, and another different synthetic broadband noise signal (incoherent with the signal of the left speaker) was played by the right speaker. Figure 2b depicts the sound spectra of both speakers, as well as the background noise signal. Both speakers have positive SNR ratios, but the left speaker emits higher $L_\mathrm{p}$ values than the right one throughout the whole frequency range of interest.

An additional recording with just the right speaker emitting sound was also performed, and the corrected averaged array signal was again taken as a reference. The challenge for this test case is to retrieve the correct $L_\mathrm{p}$ values emitted by each speaker, when both speakers are emitting sound simultaneously. The same scan grid was used as in Case I, as well as the ROI for the left speaker. The ROI for the right speaker spanned from from $x = 0.2$ m to $x = 0.4$ m and from $y = -0.05$ m to $y = 0.15$ m, with $z = 1$ m, see the dashed squares in Fig. 6.

### 3.3 Case III: Airfoil trailing–edge noise

A NACA 0018 airfoil was tested in the A–tunnel in order to investigate its turbulent boundary layer trailing edge (TBL–TE) noise emissions [12]. The wind tunnel has a contraction ratio of approximately 15 : 1 and was equipped with a nozzle with rectangular exit of 0.4 m $\times$ 0.7 m.

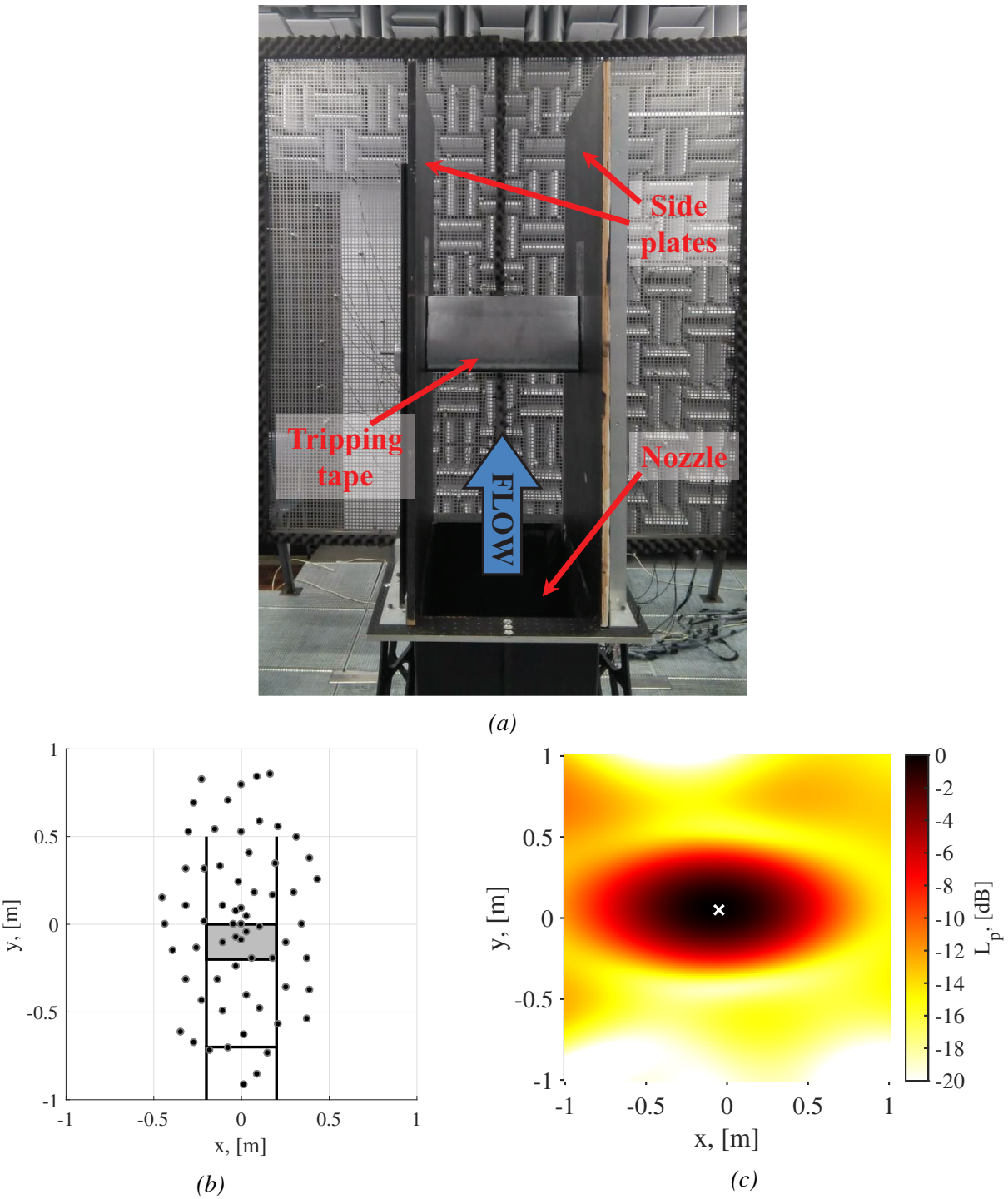


*Figure 3: (a) Picture of the NACA 0018 airfoil between the side plates in the A–-tunnel. (b) Microphone distribution of the Array 2 (seen from behind) and relative position of the airfoil (depicted as a gray rectangle and situated 1.3 m away from the array's plane). The side plates and the nozzle's exit are indicated with solid black lines. (c) PSF of the Array 2 for a point source at the left speaker location (denoted by the white × symbol) emitting sound within a 630 Hz one–third–octave band.*

The airfoil was manufactured in aluminum and has a chord of 0.2 m and a span of 0.4 m, i.e., equal to the test section's width. The airfoil was installed between two wooden plates of 1.2 m length, to approximate the two–dimensionality of the flow over most of the airfoil's span [84], see Fig. 3a. These side plates were not present for the tests with speakers.

Two freestream velocities $V$ were considered for this study: 20 m/s and 40 m/s, providing a maximum Mach number of 0.117 and a maximum chord–based Reynolds number of $5.27 \times 10^5$. Both velocities were uniform over the whole test section within 0.5% and with a turbulence intensity below 0.1% for the entire velocity range considered [75]. Since the maximum Reynolds number corresponds to the laminar flow regime, the transition to turbulent boundary layer was forced following the guidelines described in [85]. A tripping tape was used with carborundum elements with a nominal size of 0.84 mm, randomly distributed on a tape of 10 mm width, centered at 20% of the chord and covering the whole span on the pressure and suction sides of the airfoil, see Fig. 3a. The turbulent nature of the boundary layer was confirmed using a remote wall–pressure probe. The airfoil was set at a geometric angle of attack of $\alpha = 0^\circ$ for all test cases using a digital angle meter [23].

The microphone distribution for the airfoil measurements corresponds to an adapted Underbrink spiral array design [86] with 7 spiral arms of 9 microphones each, and an additional microphone located at the center of the array. This design was scaled to half its size in the $x$ direction, i.e., with approximate dimensions of 1 m $\times$ 2 m, to ensure a clear sound propagation path from the airfoil's trailing to the microphones, limiting the blocking by the side plates, see Fig. 3b, and for separating the trailing–edge noise from other potential noise sources present in the $y$ direction in an easier way. In the same plot, the relative position of the airfoil is depicted as a gray rectangle. This array is referred to as *Array 2*. The corresponding PSF [18] is illustrated in Fig. 3c, also for a point source located at the left speaker position (for comparison purposes with Fig. 1b) emitting sound within a one–third–octave frequency band centered at 630 Hz. The calculation of the synthetic PSF does not take the presence of the side plates into account. It is observed that this PSF is more elongated in the $x$ direction due to the smaller aperture of the array in that direction.

The trailing edge of the airfoil was situated at a distance of $z = 1.3$ m from the array plane and the center of the trailing edge was approximately aligned with the center microphone of the array ($x = 0$ m and $y = 0.05$ m). The leading edge of the airfoil was situated 0.5 m above the outlet of the wind–tunnel nozzle to separate potential extraneous noise sources coming from the nozzle. The signal measured by the array (averaged over all microphones) was again considered as a reference, as well as the estimations by the Brooks–Pope–Marcolini (BPM) airframe noise prediction model [87]. It should be noticed that both the averaged microphone signals and the BPM model consider the noise emissions of the whole airfoil and not just the trailing–edge noise, which is the object of interest of this study. The averaged microphone measurements also include the background noise of the wind–tunnel facility.

For all methods a scan grid ranging from $x = -0.5$ m to $x = 0.5$ m and from $y = -0.5$ m to $y = 0.5$ m was used, with $z = 1.3$ m. A spacing between grid points of $\Delta x = 0.01$ m for CFDBF, FUNBF, FPB, EHR–CLEAN–SC and GIBF, and of $\Delta x = 0.01$ m for OB, CLEAN–SC, CMF and GIBF–NNLS. The obtained source maps were integrated within a rectangular ROI spanning from $x = -0.1$ m to $x = 0.1$ m and from $y = 0$ m to $y = 0.1$ m, with $z = 1.3$ m, see dashed rectangles in Figs. 8 and 9.

# 4 RESULTS DISCUSSION

The sections below contain the main results obtained for the three experimental cases, in terms of frequency spectra and exemplary source maps. All the acoustic imaging methods described in section 2 considered. As aforementioned, GO (see section 2.9) does not provide source maps strictly speaking, but instead it offers some kind of energy landscapes [44] that are not presented here for brevity reasons. The expected source locations were found in all the cases. FPB, on the other hand, is not really an imaging method but rather an integration technique of the results provided by FUNBF. Thus, for GO and FPB, only frequency spectra results are shown.

## 4.1 Case I: Single speaker

### Source maps

Figure 4 presents one example source map obtained by each acoustic imaging method considered for the single speaker case. The results correspond to a one–third–octave frequency band centered at 630 Hz and all maps have a dynamic range of 20 dB. This frequency band was selected because it represents one of the lowest SNR cases, see Fig. 2a. The speaker signal for this frequency band is even lower than the background noise, i.e., it has a negative SNR value (about $-11.5$ dB).

The CFDBF source map is depicted in Fig. 4a and it is observed that, apart from the speaker (located approximately in the center of the plot), there are two other dominant noise sources: one at the top of the map (approximately at $x = 0.1$ m and $y = 1$ m) and another one at the bottom left corner of the map (approximately at $x = -1$ m and $y = -1$ m). Applying beamforming to a background noise recording indicated that these two sources are indeed real and part of the background noise of the wind tunnel facility, rather than being sidelobes. Apart from that, the results obtained with CFDBF show a poor spatial resolution and a high sidelobe level (about 8 dB lower than the peak level). The source map provided by FUNBF (Fig. 4b) shows a similar source distribution as the CFDBF map but with a sharper main lobe and lower sidelobe level (about 12 dB lower than the peak level). OB (Fig. 4c) presents a discontinuous source distribution for the background noise sources at the edges of the scan grid and several point sources representing the speaker. An additional weaker source is detected at $x = 0$ m and $y = -0.4$ m). In general, OB greatly improves the main lobe width and the sidelobe level with respect to CFDBF. The results of CLEAN–SC (Fig. 4d) are similar to those of OB but, in this case, the source representing the speaker is more smeared in the vertical direction. The aforementioned background noise sources and weaker source of OB are also present. EHR–CLEAN–SC (Fig. 4e) shows main lobes with a width selected by the user (in this case, larger than for the standard CLEAN–SC case). There seems to be a *floor* on this source map between 0 dB and 2 dB, which indicates that there are still remaining contributions to the CSM of the *dirty* map, after subtracting the contribution of the identified sound sources. The two aforementioned background noise sources are detected as discrete point sources. This example highlights the importance of selecting a conservative number of expected sound sources for EHR–CLEAN–SC by observing the CFDBF source map and verifying the number of dominant eigenvalues in the CSM. If only one source is considered, only the noise source at the bottom left of the map would be identified since it is the strongest source. The source map obtained with CMF (Fig. 4f) resembles those of OB and CLEAN–SC but with a larger spread and number of spurious

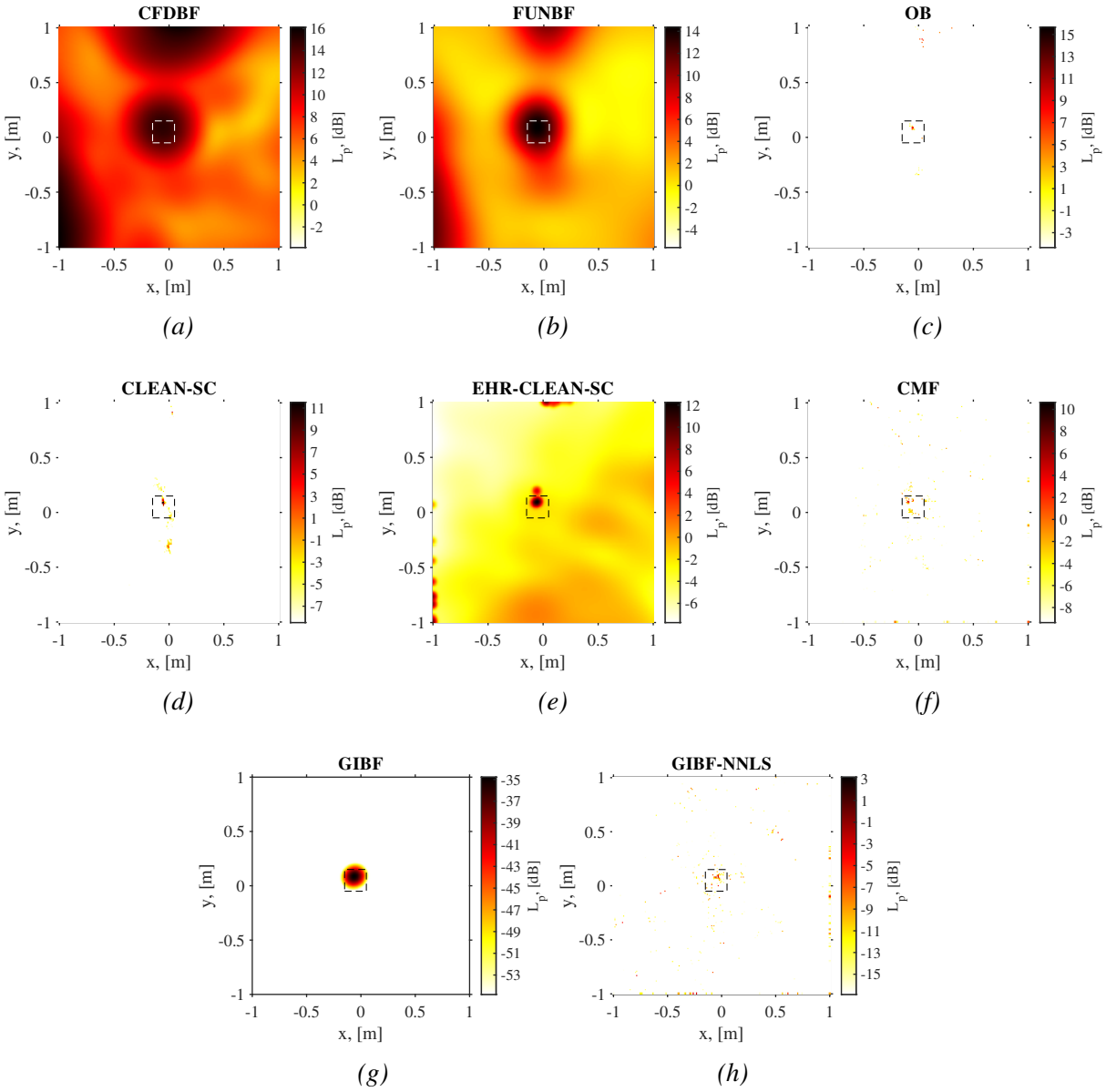


*Figure 4: Source maps for the case of a single speakers with the lowest SNR ($SNR_2$) for a one–third–octave frequency band centered at 630 Hz for: (a) CFDBF, (b) FUNBF, (c) OB, (d) CLEAN–SC, (e) EHR–CLEAN–SC, (f) CMF, (g) GIBF, and (h) GIBF–NNLS. The dashed squares denote the ROI.*

sources over the scan grid. GIBF with the regularization suggested in [70, 71] (Fig. 4g) seems to provide the cleanest results, showing the correct source location with no other secondary sources or sidelobes. This is because only the third largest eigenvalue (corresponding to the speaker) was selected for plotting. The peak levels of GIBF, however, are considerably lower than for the other methods since GIBF maps display the source distribution contours, which should be integrated, considering the assumption of source coherence as explained in section

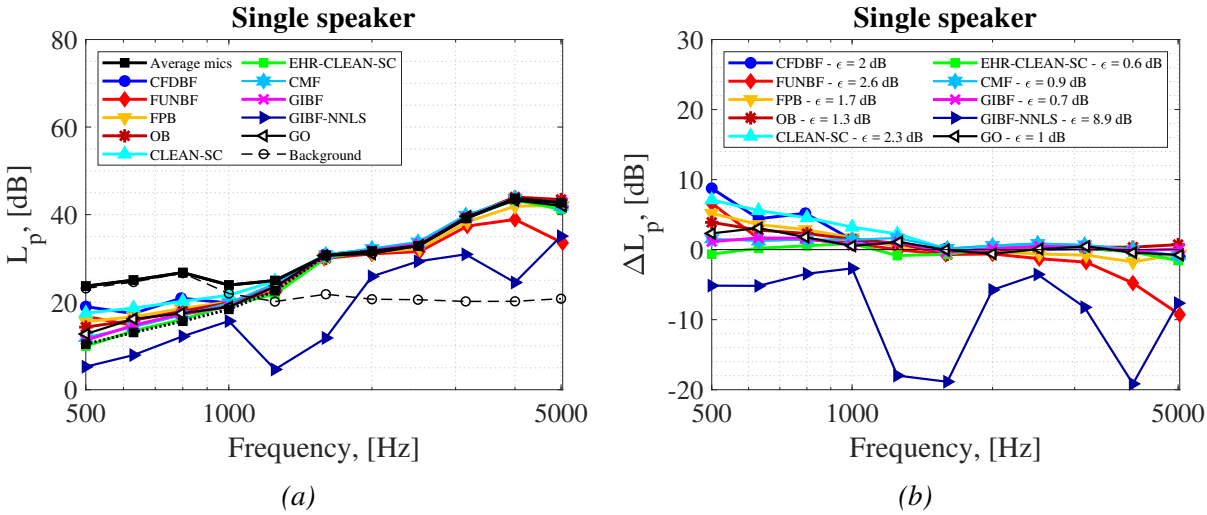


*Figure 5: (a) One–third–octave band frequency spectra for all the considered acoustic imaging methods, as well as for the average microphone signal and the background noise of the facility for the case of a single speaker with $SNR_2$. (b) Error per third–octave band made by each acoustic imaging method with respect to the average microphone signal.*

2.8. Lastly, GIBF with an NNLS solver, (Fig. 4h) shows a similar distribution as CMF, but with lower peak values.

### Frequency spectra

The sound spectra obtained by each method by integrating the source maps within the ROI are shown in Fig. 5a for all cases. The reference signal (averaged array response) is also shown, as well as the background noise spectrum of the facility. As aforementioned in section 3.1, the sound from the speaker is below the background noise of the facility for some frequency bands (approximately below 1 kHz), i.e., it has a negative SNR. For those frequency bands, all the acoustic imaging methods considered provide values below the background noise but with a larger spread between the different methods.

In order to assess the accuracy of each method in retrieving the correct sound spectra, the relative errors with respect to the reference average microphone signal $\Delta L_\mathrm{p} = L_\mathrm{p,method} - L_\mathrm{p,ref}$ were calculated. Thus, a positive value of $\Delta L_\mathrm{p}$ corresponds to an overprediction of the result by the acoustic imaging method and vice versa. The relative errors are plotted in Fig. 5b. In addition, the absolute error made by each method averaged over the whole frequency range considered (the eleven one–third–octave bands) $\varepsilon = \overline{|\Delta L_\mathrm{p}|}$ (i.e., the average $\mathscr{L}^1$ norm of the differences) is also calculated and included in the legends of Fig. 5b.

In general, the errors made by each method increase for low frequencies, where the SNR of the speaker is lowest. EHR–CLEAN–SC provides the lowest overall error with respect to the reference signal with $\varepsilon = 0.6$ dB, followed closely by GIBF (with $\varepsilon = 0.7$ dB), CMF with $\varepsilon = 0.9$ dB, and GO with $\varepsilon = 1$ dB. OB, and FPB provide $\varepsilon$ values below 2 dB and lastly, CFDBF, standard CLEAN–SC and FUNBF offer, in that order, the higher error values. FUNBF presents

a decay at the higher frequencies bands (4 and 5 kHz), which is due to the aforementioned sensitivity of this method to a mismatch in the steering vector when coarse grids are used (see section 2.2). This can be solved by employing a finer grid [30] with the consequently higher computational time. GIBF–NNLS seems to provide consistently lower estimates and has an average error of about 9 dB. The reason for this relatively large offset remains unknown, but it could be because this technique localizes the dominant sound sources outside of the ROI.

### 4.2 Case II: Two speakers

#### Source maps

Figure 6 contains one example source map obtained for the case with two speakers by each of the methods considered. These results also correspond to a one–third–octave frequency band centered at 630 Hz. This frequency band was selected because for the given array geometry and distance between sources (0.35 m), it approximately represents the Rayleigh resolution limit frequency ($\sim$ 645 Hz) for which the two sources can be distinguished using conventional acoustic imaging methods. The sound pressure levels emitted by both speakers are practically identical for these conditions, see Fig. 2b.

The source map obtained by CFDBF (Fig. 6a) shows an elongated sound source with a peak between the actual positions of both speakers, due to the insufficient spatial resolution of this method at this frequency. There are still some sidelobes present in the source map, about 14 dB lower than the peak level. FUNBF (Fig. 6b) removes the sidelobes from the CFDBF source map and just distinguishes both speakers as separate sound sources. Distinguishing both sources becomes easier if the exponent parameter $\nu$ of this method is increased, at the risk of stronger instabilities at high frequencies [37]. OB (Fig. 6c) presents no sidelobes but some discontinuous line source in between the speakers. In addition, the peak $L_\mathrm{p}$ value is about 9 dB lower than the one of CFDBF. A similar source distribution is obtained by standard CLEAN–SC (Fig. 6d), but with the levels more concentrated at the speakers' locations. EHR–CLEAN–SC (Fig. 6e) performs best for this case clearly separating both speakers with the correct $L_\mathrm{p}$ values and showing only a sidelobe about 20 dB lower than the peak value. The results obtained by CMF (Fig. 6f) show the main sources around the speakers' locations but also some additional secondary sources outside of the ROIs considered. The results obtained by GIBF (Fig. 6g) depict a somehow distributed line source with maximum levels at both ends of the segment, slightly further away than the actual positions of the speakers. Lastly, GIBF with the NNLS solver (Fig. 6h) shows the maximum levels between the two speakers and some additional secondary sources outside of the defined ROIs.

#### Frequency spectra

In a similar way as it was done for the single speaker case, the integrated spectra within the two ROIs depicted in Fig. 6 were compared, respectively, to the reference signals of the left and right speaker recorded by the array and averaged over all microphones and corrected for the distance of 1 m to the sound source (with only one speaker emitting in that case).

As explained in section 3.2, the left speaker was set to emit the exact same synthetic broadband noise signal as in the $\mathrm{SNR}_1$ case and the right speaker emitted the a different incoherent synthetic broadband signal. Figure 7a presents the resulting average one–third–octave band

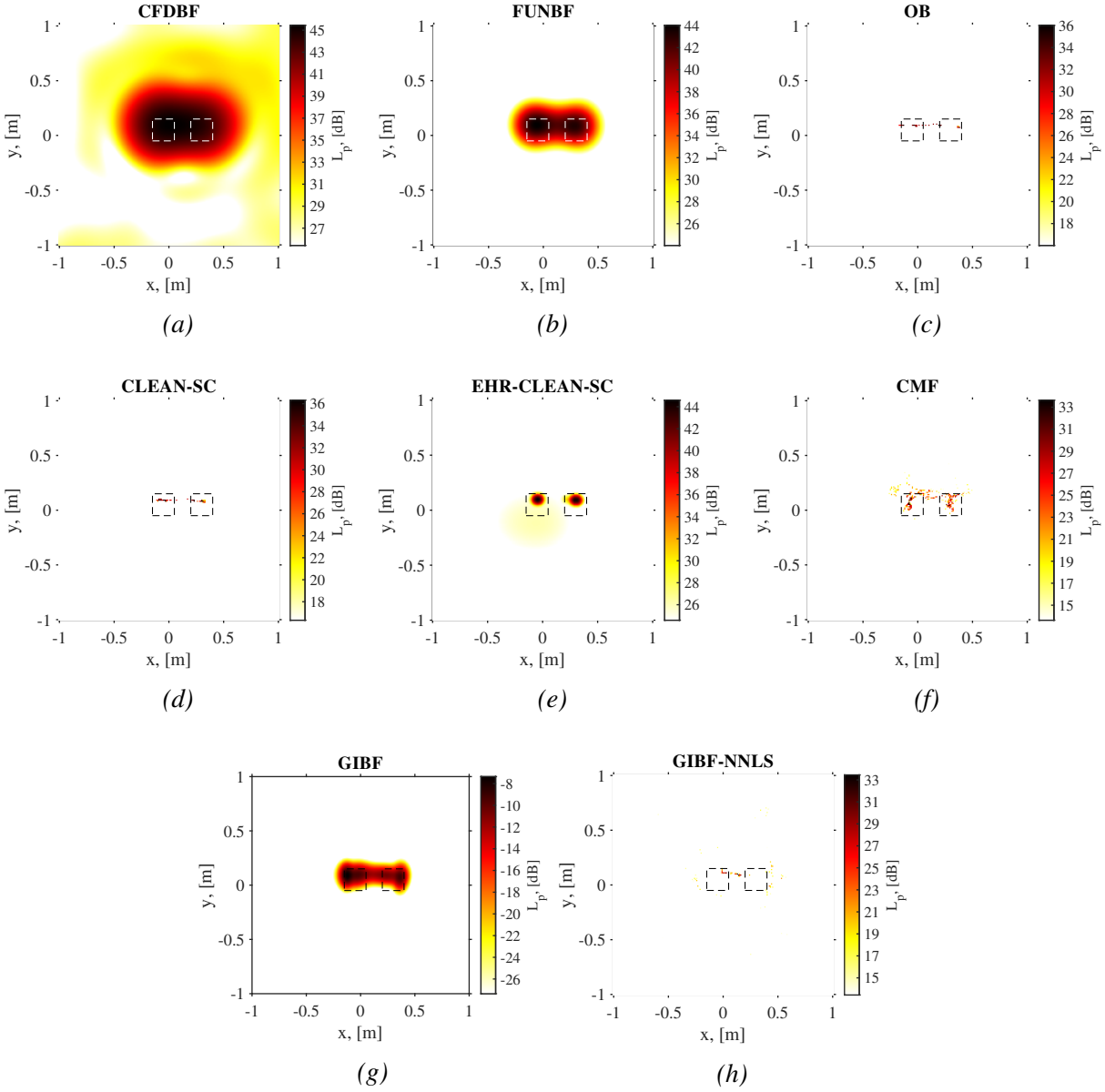


*Figure 6: Source maps for the case of two speakers for a one–third–octave frequency band centered at 630 Hz for: (a) CFDBF, (b) FUNBF, (c) OB, (d) CLEAN–SC, (e) EHR–CLEAN–SC, (f) CMF, (g) GIBF, and (h) GIBF–NNLS. The dashed squares denote the ROIs.*

spectra for the left speaker. The Rayleigh resolution limit for the given setup ($\sim$ 645 Hz) is also denoted as a vertical dotted black line. The respective relative errors $\Delta L_\mathrm{p}$ with respect to the reference signal are presented in Fig. 7b. In general, GIBF shows the best results for this case (with $\varepsilon = 0.3$ dB), followed by GO (with $\varepsilon = 0.8$ dB), CMF (with $\varepsilon = 0.9$ dB), and CLEAN-SC and EHR–CLEAN–SC both with $\varepsilon = 1$ dB. FPB and OB provide acceptable results with

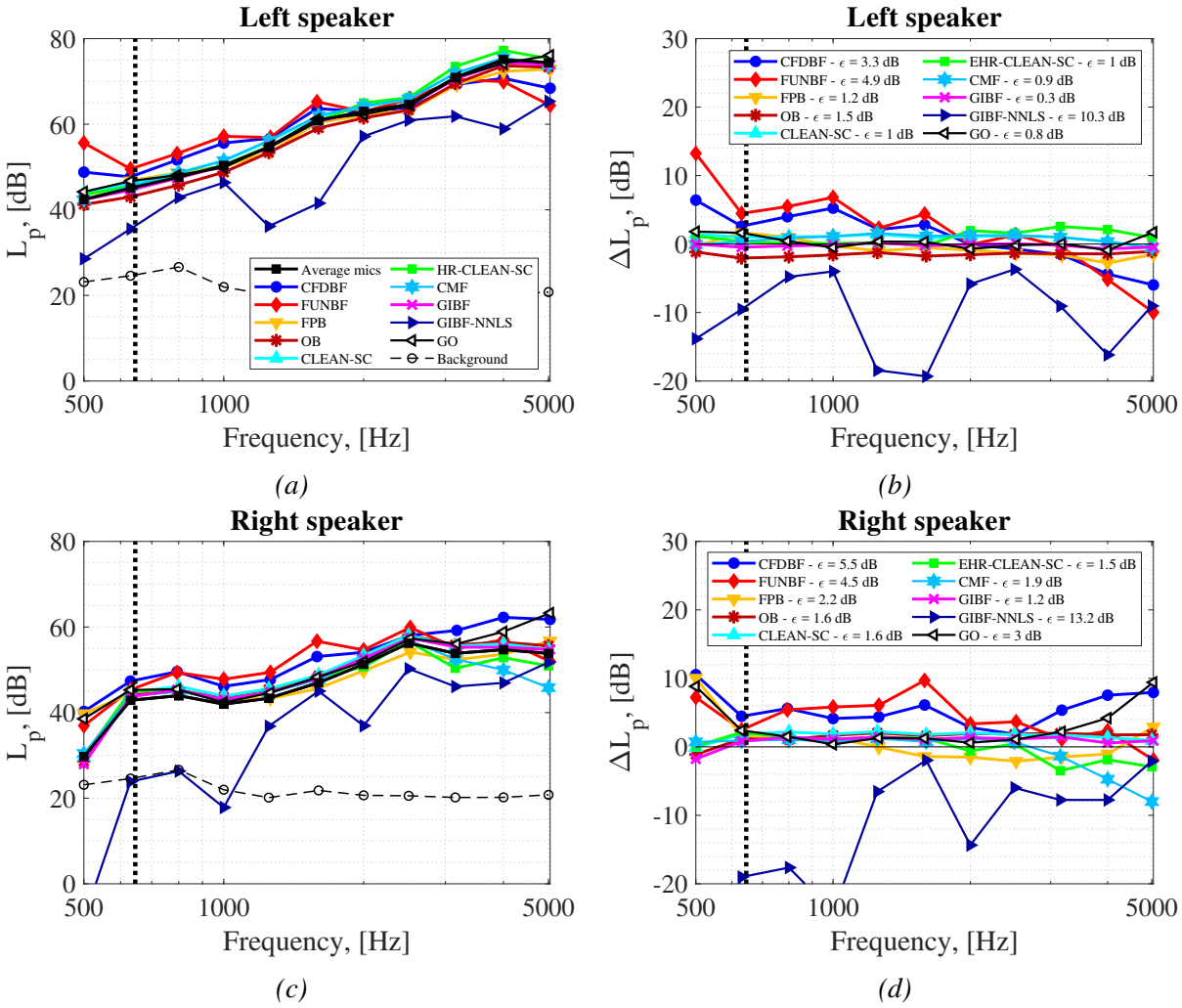


*Figure 7: Left column: One–third–octave band frequency spectra for the case with two speakers for all the considered acoustic imaging methods, as well as for the average microphone signal and the background noise of the facility for the case with two speakers. Right column: Error per third–octave band made by each acoustic imaging method with respect to the average microphone signal. The rows refer to each speaker: (a) and (b) left speaker, (c) and (d) right speaker.*

$\varepsilon \leq 1.5$ dB. CFDBF and FUNBF show a consistent large overestimation of the levels for the lower part of the frequency range, with the additional aforementioned decay at high frequency for FUNBF. CFDBF makes average errors of $\varepsilon = 3.3$ dB whereas for FUNBF it increases up to almost 5 dB. Once again, GIBF–NNLS provide consistently lower values throughout the whole frequency range and makes an average error of 10.3 dB.

The obtained spectra for the right speaker is presented in Fig. 7c and the $\Delta L_p$ with respect to the reference signal in Fig. 7d. Overall, all methods (except for FUNBF) present higher values of $\varepsilon$ than for the left speaker case, which is expected because the right speaker was the weaker source, see Fig. 2b. Once again, GIBF seems to make the smallest errors for this

case (with $\varepsilon = 1.2$ dB) followed closely by EHR–CLEAN–SC (with $\varepsilon = 1.5$ dB) and standard CLEAN–SC and OB, both of them with $\varepsilon = 1.6$ dB. CMF makes an average error or 1.9 dB for this case. FPB shows a considerably large error for the lowest frequency band (500 Hz) that causes its error to increase to $\varepsilon = 2.2$ dB. GO provides relatively good performance for most of of the frequency spectrum, but it overestimates the results for the two lowest and two highest frequency bands, which increases the error made to 3 dB . For this case, FUNBF presents better results ($\varepsilon = 4.5$ dB) than CFDBF ($\varepsilon = 5.5$ dB) and does not present the high frequency decay. It is however, CFDBF that shows a large overestimation of the results at high frequencies. This is probably due to the relatively low levels emitted by the right speaker in comparison with the left speaker for that frequency range (about than 20 dB lower), see Fig. 2b. In fact, observing the source maps at those frequencies (not included in this paper), the sidelobes due to the presence of the left speaker are stronger than the right speaker, and those sidelobes are included in the integration of the ROI. Lastly, GIBF–NNLS increases its error even more for the right speaker providing an average error of 13.2 dB.

### 4.3 Case III: Airfoil trailing–edge noise

#### Source maps

Two sets of source maps for the NACA 0018 airfoil are presented in Figs. 8 and 9 for illustration purposes. All the maps have a dynamic range of 20 dB and consider the convection of the sound due to the presence of flow [14].

The first case corresponds to a flow velocity of 40 m/s and a one–third–octave frequency band centered at 1 kHz. This case had a SNR of approximately 5 dB with respect to the background noise of the wind tunnel at that flow velocity without the airfoil present [30]. The CFDBF source map (Fig. 8a) depicts a distributed sound source along the trailing edge, but also extraneous noise sources coming from the collector and the nozzle of the wind tunnel, located at the top and the bottom of the picture, respectively. FUNBF (Fig. 8b) improves the results to some extent by narrowing the width of the line source at the trailing edge and separating the extraneous noise sources slightly further. The source map of OB (Fig. 8c) presents a main point source in the middle of the trailing edge and some weaker spurious sources outside of the ROI. Once again, the peak values in this case are about 9 dB lower than those of CFDBF. Standard CLEAN–SC (Fig. 8d) provides a similar source distribution as OB but with two point sources located approximately at the junctions of the trailing edge of the airfoil with the side plates. EHR–CLEAN–SC (Fig. 8e) provides a cluster of sound sources somewhat distributed in the vicinity of the trailing edge and mostly concentrated in the middle of the edge. The extraneous noise sources are basically eliminated but few additional point sources are unexpectedly found upstream of the trailing edge (at about 60% of the airfoil chord). This method shows again a *noise floor* about 20 dB lower than the peak value. CMF (Fig. 8f) presents a larger spread in the location of the sound sources, with some of the strongest sources detected outside of the ROI. GIBF (Fig. 8g) shows a slightly elongated sound source located at the center of the trailing edge, without any other sound sources present. Lastly, GIBF with the NNLS solver (Fig. 8h) presents a discontinuous distribution of sources with the higher values inside or near the ROI and a cluster of secondary sources at approximately $x = 0.4$ m and $y = 0$ m.

The second example refers to the other flow velocity (20 m/s) and a one–third–octave frequency band centered at 4 kHz. This case had a SNR of approximately 8 dB with respect to the

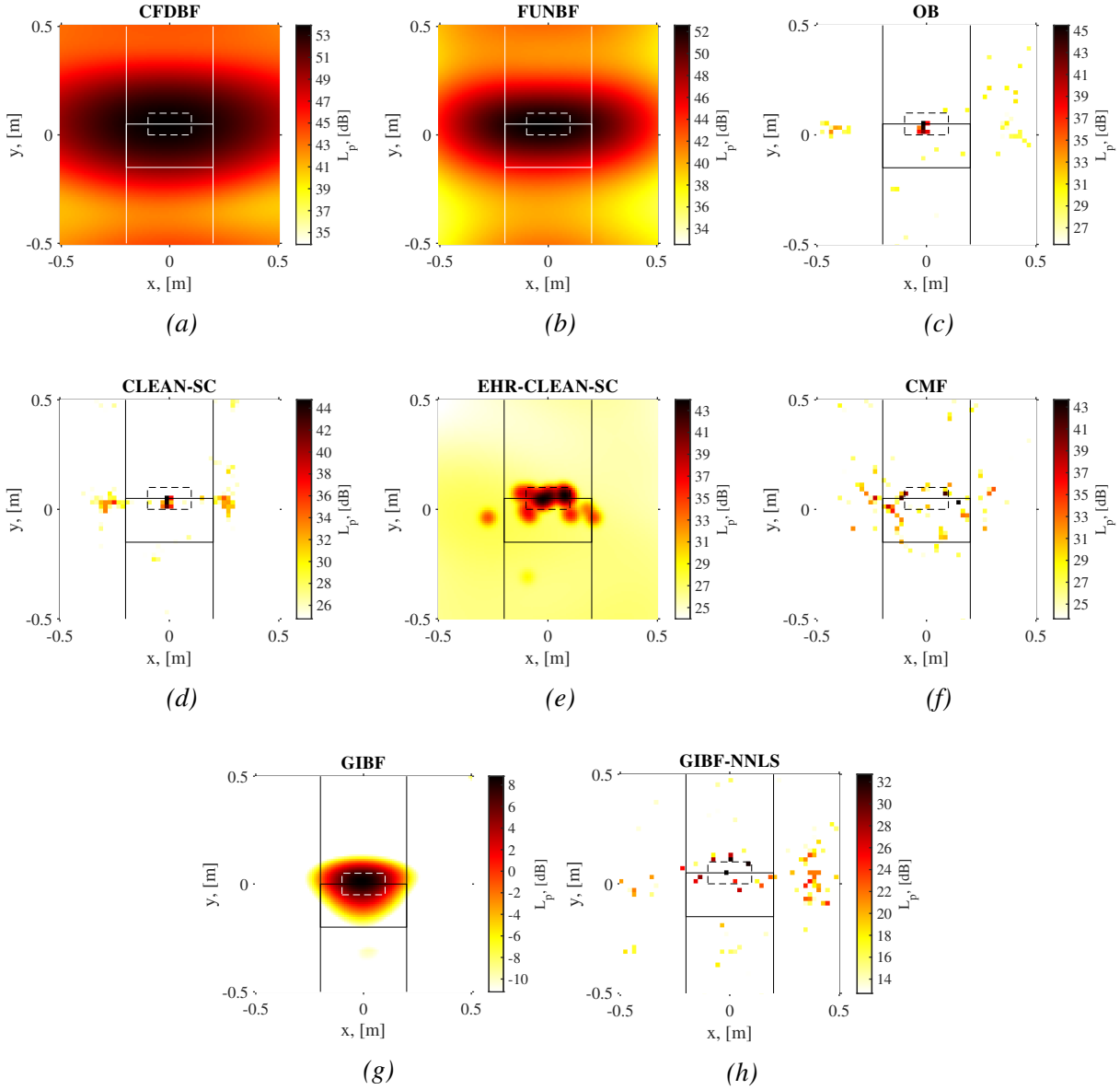


*Figure 8: Source maps for the NACA 0018 airfoil with $V = 40$ m/s for a one–third–octave frequency band centered at 1 kHz for: (a) CFDBF, (b) FUNBF, (c) OB, (d) CLEAN–SC, (e) EHR–CLEAN–SC, (f) CMF, (g) GIBF, and (h) GIBF–NNLS. The airfoil location and side plates are denoted by a solid rectangle and vertical lines, respectively. The dashed rectangles denote the ROI.*

background noise of the wind tunnel at that flow velocity without the airfoil present [30]. These conditions were selected because the contribution of the leading–edge noise was observed to be dominant compared to the trailing–edge noise [30]. The exact cause for having the leading edge noise as a dominant source at the conditions of the current experiment is not known with certainty yet since this type of source is normally generated due to the incoming turbulence of

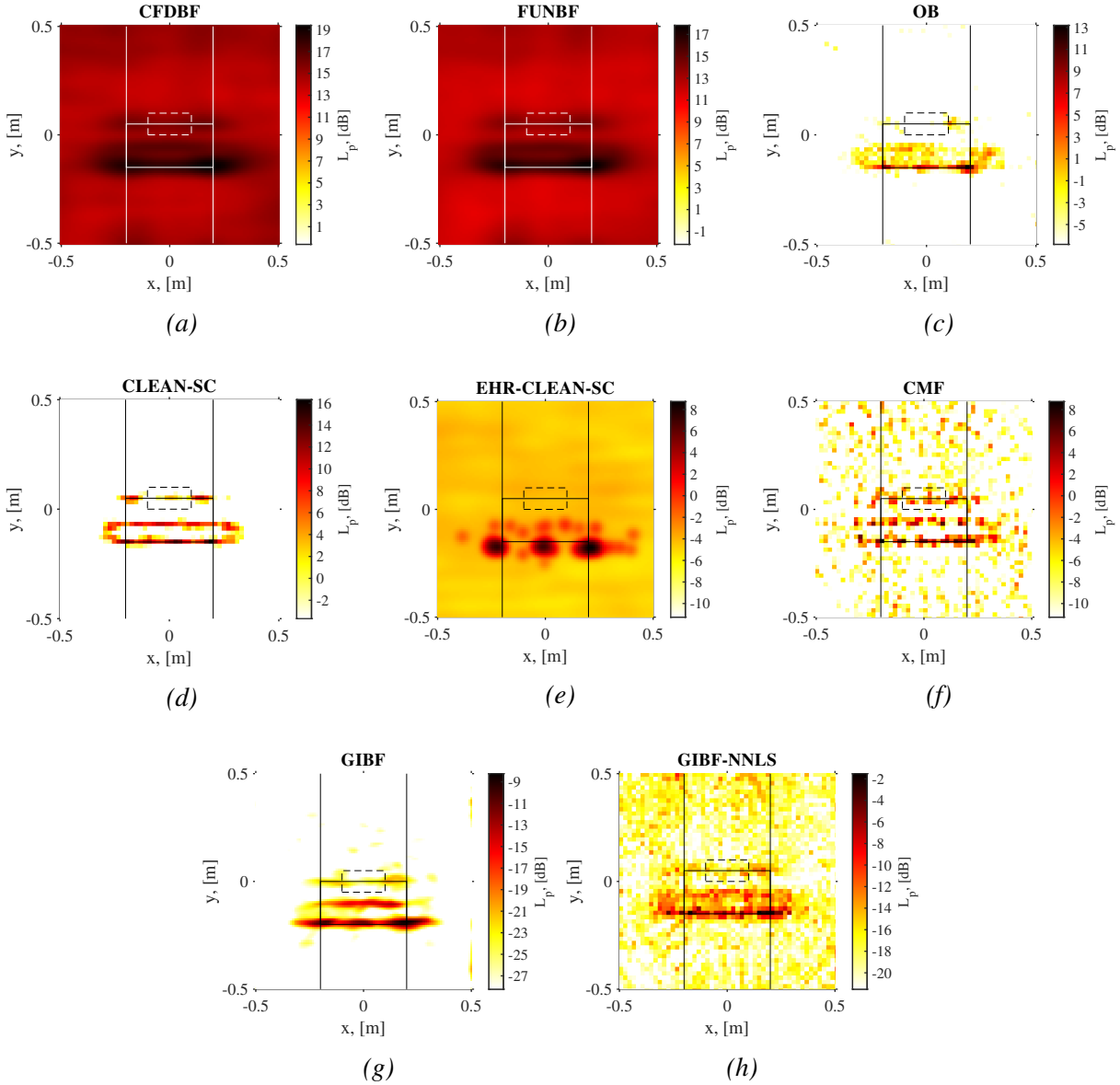


*Figure 9: Source maps for the NACA 0018 airfoil with $V = 20$ m/s for a one–third–octave frequency band centered at 4 kHz for: (a) CFDBF, (b) FUNBF, (c) OB, (d) CLEAN–SC, (e) EHR–CLEAN–SC, (f) CMF, (g) GIBF, and (h) GIBF–NNLS. The airfoil location and side plates are denoted by a solid rectangle and vertical lines, respectively. The dashed rectangles denote the ROI.*

the flow [87] and the turbulence intensity levels for the wind tunnel used are below 0.1%. A possible cause of this noise source could be the tripping tape mentioned in section 3, placed at 20% of the chord. The nominal size of the carborundum elements used in this paper was 0.84 mm, instead of 0.6 mm as in other previous experiments in the same wind tunnel that did not present dominant leading–edge noise [80–83]. Hence, this increase in roughness is probably

the generating mechanism for leading–edge noise in this experiment.

The source map obtained from CFDBF (Fig. 9a) shows the presence of the leading edge noise as a dominant noise source followed by what seems to be another line source at about 40% of the airfoil chord, which could be due to some flow instabilities at that location. This second line source is, however, not clearly distinguishable due to the insufficient spatial resolution of this method. The trailing edge noise is also present as a secondary line source. In general, for both the leading–edge and trailing–edge noise sources, the peak values are located in the junction with the vertical side plates (i.e., at $x = \pm 0.2$ m). The reason for this is likely the interaction of the boundary layer of the vertical side plates with the corners of the airfoil [88]. The influence of these corner sources is minimized by integrating the results within the selected ROI. FUNBF (Fig. 9b) slightly improves the sidelobe level with respect to CFDBF but it shows a very similar source distribution. The sidelobe level could be further improved by removing the main diagonal of the CSM [14] but it was observed that this approach can lead to misleading results at high frequencies. For example, if the leading–edge noise source is stronger than the trailing–edge noise, the presence of the former can reduce the observed values of the latter, especially when using methods that rely on the eigenvalue decomposition of the CSM, such as FUNBF. An extended explanation of this phenomenon can be found in [18]. OB (Fig. 9c) does not seem to detect the trailing–edge noise source and only detects the leading–edge noise and the secondary source at about 40% of the airfoil chord. In this case, standard CLEAN–SC (Fig. 9d) manages to successfully separate the three line sources (leading– and trailing–edge and the secondary source) without any other major noise sources outside of the airfoil. Once again, EHR–CLEAN–SC (Fig. 9e) displays a discontinuous distribution of sound sources, with the presence of two dominant point sources located at the corners of the airfoil at the leading edge and one in the center of the leading edge. A number of secondary sound sources are also detected at about 40% of the chord and along the whole span. The trailing–edge noise source, however, is not detected in this case. CMF (Fig. 9f) provides a similar source distribution as standard CLEAN–SC but considerably more contaminated by spurious sources all over the scan grid. GIBF (Fig. 9g) clearly shows the leading–edge as the dominant noise source, as well as the secondary source at 40% of the chord, and a weaker source for the trailing–edge noise. Lastly, GIBF–NNLS (Fig. 9h) presents a similar source distribution as GIBF, but considerably more contaminated by sidelobes.

### Frequency spectra

The source maps obtained by all the acoustic imaging methods were integrated within the defined ROI to isolate the trailing–edge noise frequency spectra. The integrated results in the ROI considered (with a spanwise length of 0.2 m) were scaled to account for the full span of the airfoil (0.4 m) by adding 3 dB (double power), since the airfoil span is twice the one of the ROI.

The obtained frequency spectra are presented in Fig. 10, as well as for the signal recorded by the array (averaged over all microphones), the estimations of the BPM method [87] and the background noise of the facility (at the corresponding velocities and without the airfoil present). The BPM model is a semi–empirical model for predicting various components of airfoil self–noise, including the turbulent boundary trailing edge noise. The results can be extended to different airfoil geometries, such as for the NACA 0018 case analyzed here [30]. This model provides the predicted noise spectra in one–third–octave bands based on the given Reynolds number, effective angle of attack, airfoil's chord and span, and the observer's location. The

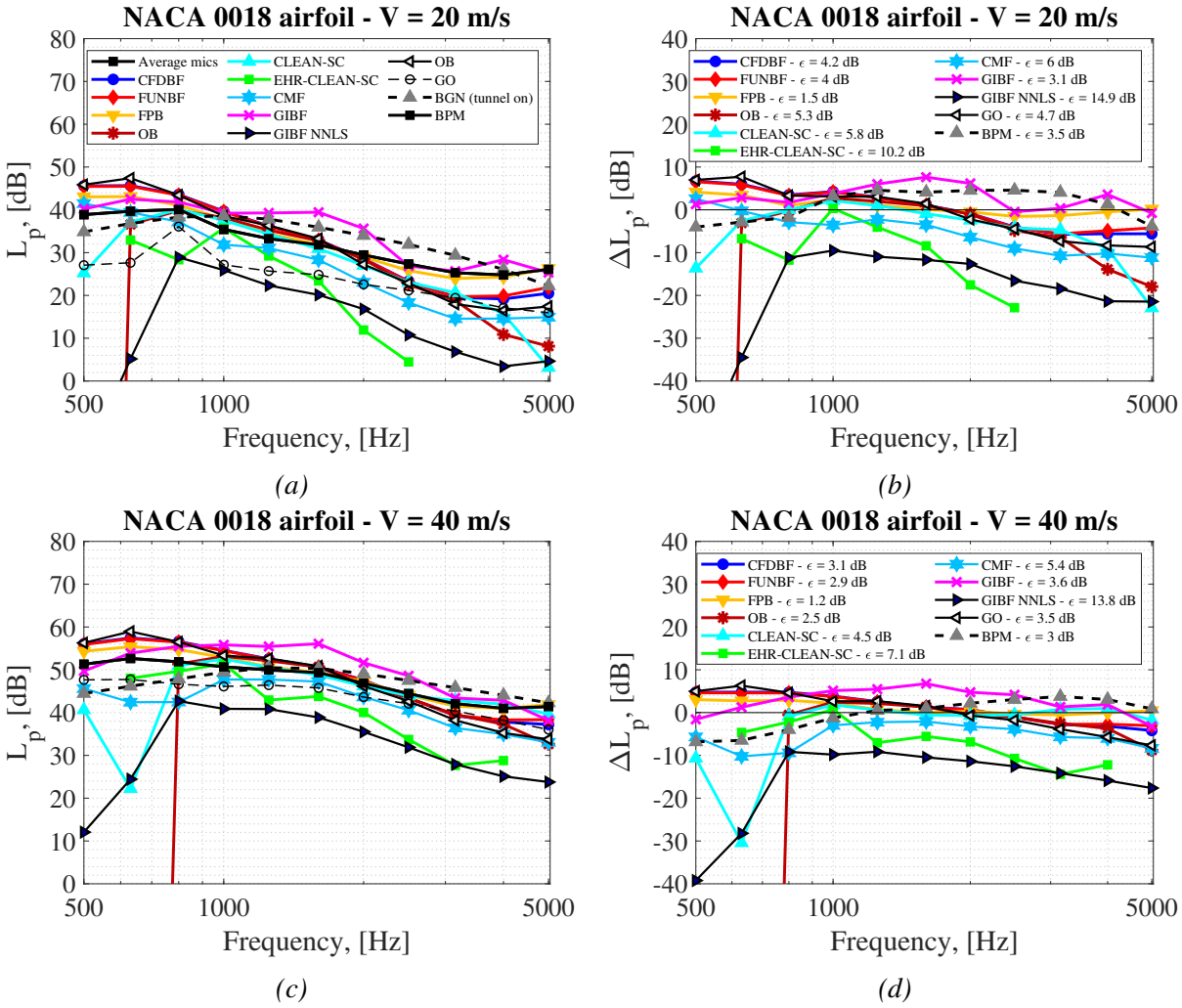


*Figure 10: Left column: One–third–octave band frequency spectra for the NACA 0018 airfoil for all the considered acoustic imaging methods, as well as for the signal recorded by the array (averaged over all microphones), the estimations of the BPM method and the background noise of the facility. Right column: Error per third–octave band made by each acoustic imaging method, with respect to the average microphone signal. The rows refer to different flow velocities: (a) and (b) $V = 20$ m/s, (c) and (d) $V = 40$ m/s.*

displacement thickness of the boundary layer $\delta^*$ is an optional input. In this case, the values for $\delta^*$ for the NACA 0018 airfoil were estimated using the software XFOIL [89] and were found to be 2.3 mm for $V = 20$ m/s and 2.1 mm for $V = 40$ m/s. The spectra for both flow velocities considered are included: 20 m/s (Fig. 10a) and 40 m/s (Fig. 10c). All the spectra correspond to an observer distance of 1 m from the trailing edge.

On the right in Fig. 10, the differences in sound pressure level $\Delta L_p$ with respect to the reference spectrum measured by the array (averaged over all microphones) are depicted. It should be noted that the average signal measured by the array is not just due to the trailing–

edge noise but also from other extraneous sources, such as the leading–edge noise (see Fig. 9). However, for the given setup, trailing–edge noise is expected to be the dominant noise source for most of the frequency range [87].

In general, all the acoustic imaging methods employed show a similar trend as the average microphone signal, except for EHR–CLEAN–SC, which provides considerably lower values and even no results for some frequency bands, for which no sources were resolved within the selected ROI because they fell outside of it. This behavior can be explained because this method specifically considers the presence of point sources (five in this case), instead of distributed sources as trailing–edge noise. GIBF–NNLS shows a somehow constant offset of about $-10$ dB for most of the frequency range, and unstable behavior for the two lowest frequency bands (500 Hz and 630 Hz). This erratic behaviour for the low frequencies is also seen in the case of OB. Those outliers were omitted for calculating $\varepsilon$. FPB seems to provide the smallest differences with respect to the reference signal in this case with $\varepsilon \leq 1.5$ dB. This method is followed by GIBF and the BPM prediction model with $\varepsilon \approx 3.5$ dB. FUNBF, CFDBF, GO, and OB show (in that order) slightly higher average differences up to about 5 dB. CLEAN–SC and CMF provide higher $\varepsilon$ values but still lower than EHR–CLEAN–SC and GIBF–NNLS.

In general, the overall agreement for the higher flow speed (40 m/s) is closer than for the lower one (20 m/s). This could be due to the higher SNR for the higher velocity case. The divergent behaviour of OB and GIBF–NNLS at low frequencies is also present for the case of 40 m/s.

The general overestimation of the spectra by GIBF could be because the same regularization approach as for the cases with speakers was employed, which increases the intensity of the spurious sources of the map [30]. A dedicated selection of the regularization parameters is expected to improve the results [70, 71]. In a similar manner, GO assumed the presence of point sources for this analysis, but considering a more physically accurate representation of the source (such as a line source in the airfoil case) in the optimization process would likely lead to better outcomes [50]. These considerations are left for future work.

### 4.4 Summary of the errors for each case

In order to summarize the main results regarding source power estimation of the three test cases in a single figure, Fig. 11a presents a bar plot of the average errors $\varepsilon$ made by each acoustic imaging method for the experiments featuring: one speaker, two speakers and the NACA 0018 airfoil. It should be reminded that these errors are with respect to the signal measured by the average microphone, and that implies some limitations that have been mentioned throughout the text. The average errors displayed in the bar plot in Fig. 11a have been calculated by averaging linearly the errors of all the *subcases* analyzed, i.e., the left and right speakers for the two–speaker case, and both flow velocities for the NACA 0018 airfoil case.

In general, it can be observed that GIBF and EHR–CLEAN–SC are the best methods for the cases involving point sources (i.e., speakers). GIBF provides slightly lower average errors and EHR–CLEAN–SC shows a better rendering of the source maps for the case with two speakers placed closer than the Rayleigh resolution limit. For the airfoil case FPB provide the best agreement with the reference signal, whereas CFDBF, FUNBF, CLEAN–SC and GIBF render the expected line source distribution.

Moreover, since for the NACA 0018 airfoil case neither the signal of the average microphone signal nor the estimations of the BPM model can be considered as a perfect reference to compare

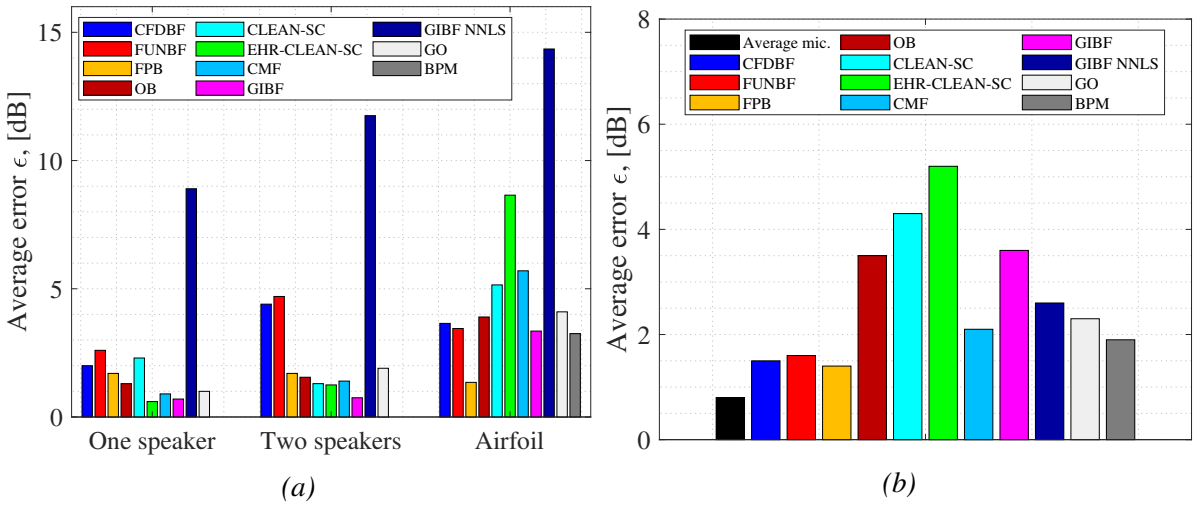


*Figure 11: (a) Average errors ε made by each of the acoustic imaging methods considered for the three experimental cases analyzed. (b) Average collapse error for the expected Strouhal scaling for trailing–edge noise.*

the results with because they also include the contribution of the leading–edge noise, it was decided to assess the expected collapse of the spectra corresponding to both flow velocities once they have their frequency axis normalized using the Strouhal number based on $\delta^*$, $St = f\delta^*/V$ and the sound pressure levels normalized by the following expression [87, 90, 91]:

$$L_{\mathrm{p,norm}} = L_{\mathrm{p}} - 10n\log_{10}\frac{V}{V_{\mathrm{ref}}} - 10\log_{10}\frac{\delta^*}{\delta^*_{\mathrm{ref}}} \tag{28}$$

where $V_{\mathrm{ref}}$ is a reference velocity, and $\delta^*_{\mathrm{ref}}$ and $L_{p,V_{\mathrm{ref}}}$ are the displacement thickness of the boundary layer (estimated using XFOIL [89]: 2.3 mm for $V = 20$ m/s and 2.1 mm for $V = 40$ m/s) and the sound pressure level at that same velocity, respectively. The parameter $n$ is the expected dependency of the trailing–edge noise levels with respect to the flow velocity $V$. For this assessment, a value of $n = 4.5$ was used, following the suggestions from literature [87, 90, 91]. The agreement between the scaled spectra at both flow velocities using the normalization of Eq. (28) is illustrated as a bar plot in Fig. 11b. Overall, the best collapse of the two normalized spectra is found for the case of the average microphone signal, where an average deviation $\varepsilon$ within the frequency range considered of 0.8 dB is observed. After that, FPB, CFDBF and FUNBF present the closest match between both scaled spectra with $\varepsilon \leq 1.5$ dB, which is a similar value as the one of the BPM model. This assessment is only complementary to the analysis performed in Fig. 10, since it can occur that a method provides a good collapse when considering the Strouhal scaling but relatively large deviations with respect to the reference signal, such as GIBF–NNLS.

In general, similar results were obtained in a benchmark exercise of a simulated line source modeling a trailing–edge noise measurement in a closed–section wind tunnel [27, 49, 50].

## 5 CONCLUSIONS

The performance of Functional Projection Beamforming (FPB) was investigated in this paper for the purpose of aeroacoustic measurements featuring microphone arrays, and compared (in terms of accuracy for retrieving the source levels) with other well–known acoustic imaging methods.

Three different experimental test cases were measured inside of an anechoic wind tunnel and analyzed using each method: 1) one speaker emitting synthetic broadband noise at low signal to noise ratio with respect to the background noise, 2) two closely–located speakers emitting incoherent synthetic broadband noise signals at different relative volumes and 3) trailing–edge noise of a tripped NACA 0018 airfoil.

Overall, it was shown that FPB presents a comparable performance to more elaborated methods for the cases featuring speakers, such as orthogonal beamforming (OB), CLEAN–SC (and its high resolution version), and generalized inverse beamforming (GIBF). Additionally, FPB does not present the sensitivity of functional beamforming (FUNBF) to a mismatch in the steering vector, which may occur when a coarse grid is employed.

For the case of distributed sources such as the trailing–edge noise of the NACA 0018 airfoil, FPB seems to provide the smallest differences with respect to the reference signal, as well as the closest agreement with the expected Strouhal scaling for trailing–edge noise (with average errors below 1.5 dB). Therefore, FPB could potentially have extensive application in aeroacoustic experiments, such as airframe or jet noise tests.

## References

[1] B. Owen, D. S. Lee, and L. Lim, *Flying into the Future: Aviation Emission Scenarios to 2050,* Environmental Science & Technology, American Chemical Society **44**, 2255 (2010).

[2] R. Merino-Martinez, S. J. Heblij, D. H. T. Bergmans, M. Snellen, and D. G. Simons, *Improving Aircraft Noise Predictions by Considering the Fan Rotational Speed,* Journal of Aircraft **56**, 284 (2019).

[3] R. Merino-Martinez, M. Snellen, and D. G. Simons, *Calculation of the fan rotational speed based on flyover recordings for improving aircraft noise prediction models,* in 23rd *International Congress on Acoustics, September 9 – 13 2019, Aachen, Germany* (2019).

[4] M. Snellen, R. Merino-Martinez, and D. G. Simons, *Assessment of aircraft noise sources variability using an acoustic camera,* in 5th *CEAS Air & Space Conference, Challenges in European Aerospace, September 7 – 11 2015, Delft, Netherlands*, 2015–019 (Council of European Aerospace Societies, Rue du Trone 98 – 1050 Brussels, Belgium, 2015).

[5] M. Snellen, R. Merino-Martinez, and D. G. Simons, *Assessment of noise level variability on landing aircraft using a phased microphone array,* Journal of Aircraft **54**, 2173 (2017).

[6] S. Oerlemans, P. Sijtsma, and B. Méndez López, *Location and Quantification of Noise Sources on a Wind Turbine,* Journal of Sound and Vibration **299**, 869 (2007).

[7] R. Merino-Martinez, R. Pieren, M. Snellen, and D. G. Simons, *Assessment of the sound quality of wind turbine noise reduction measures,* in 26th *International Congress on Sound and Vibration, July 7 – 11 2019, Montreal, Canada* (International Inst. of Acoustics and Vibration (IIAV), Auburn, Alabama, USA., 2019).

[8] L. C. Caldas, P. C. Greco, C. C. J. Pagani, and L. A. Baccalá, *Comparison of different techniques for rotating beamforming at the university of São Paulo fan rig test facility,* in 6th *Berlin Beamforming Conference, February 29 – March 1 2016, Berlin, Germany* (GFaI, e.V., Berlin, 2016) BeBeC–2016–D14.

[9] G. Herold and E. Sarradj, *Frequency domain deconvolution for rotating sources on an axial fan,* in 6th *Berlin Beamforming Conference, February 29 – March 1 2016, Berlin, Germany* (GFaI, e.V., Berlin, 2016) BeBeC–2016–D18.

[10] T. Sinnige, B. Della Corte, R. de Vries, F. Avallone, R. Merino-Martinez, D. Ragni, G. Eitelberg, and L. L. M. Veldhuis, *Alleviation of Propeller–Slipstream–Induced Unsteady Pylon Loading by a Flow–Permeable Leading Edge,* Journal of Aircraft **56**, 1214 (2019), DOI: 10.2514/1.C035250.

[11] R. Zamponi, P. Chiariotti, G. Battista, C. Schram, and P. Castellini, *3D Generalized Inverse Beamforming in wind tunnel aeroacoustic testing: application to a Counter Rotating Open Rotor aircraft model,* Applied Acoustics **163**, 1 (2020).

[12] R. Merino-Martinez, *Microphone arrays for imaging of aerospace noise sources*, Ph.D. thesis, Delft University of Technology (2018), ISBN: 978–94–028–1301–2.

[13] T. Mueller, *Aeroacoustic Measurements* (Springer Science & Business Media, Berlin, Germany, 2002) p. 313, ISBN: 978–3–642–07514–8.

[14] P. Sijtsma, *Phased array beamforming applied to wind tunnel and fly–over tests*, Tech. Rep. NLR–TP–2010–549 (National Aerospace Laboratory (NLR), Anthony Fokkerweg 2, 1059 CM Amsterdam, P.O. Box 90502, 1006 BM Amsterdam, The Netherlands, 2010).

[15] U. Michel, B. Barsikow, J. Helbig, M. Hellmig, and M. Schüttpelz, *Flyover noise measurements on landing aircraft with a microphone array,* in 4th *AIAA/CEAS Aeroacoustics Conference, June 2 – 4 1998, Toulouse, France* (1998) AIAA paper 1998–2336.

[16] R. Merino-Martinez, M. Snellen, and D. G. Simons, *Determination of Aircraft Noise Variability Using an Acoustic Camera,* in 23rd *International Congress on Sound and Vibration, July 10 – 14 2016, Athens, Greece* (International Inst. of Acoustics and Vibration (IIAV), Auburn, Alabama, USA., 2016).

[17] U. Michel, *History of acoustic beamforming,* in *Proceedings on CD of the* 1st *Berlin Beamforming Conference, 22 – 23 November, 2006* (GFaI, e.V., Berlin, 2006).

[18] R. Merino-Martinez, P. Sijtsma, M. Snellen, T. Ahlefeldt, J. Antoni, C. J. Bahr, D. Blacodon, D. Ernst, A. Finez, S. Funke, T. F. Geyer, S. Haxter, G. Herold, X. Huang, W. M. Humphreys, Q. Leclère, A. Malgoezar, U. Michel, T. Padois, A. Pereira, C. Picard, E. Sarradj, H. Siller, D. G. Simons, and C. Spehr, *A review of acoustic imaging methods using*

*phased microphone arrays (part of the Aircraft Noise Generation and Assessment special issue), CEAS aeroacoustic journal*, CEAS Aeronautical Journal **10**, 197 (2019), DOI: 10.1007/s13272-019-00383-4.

[19] P. Castellini and M. Martarelli, *Acoustic beamforming: Analysis of uncertainty and metrological performances,* Mechanical Systems and Signal Processing **22**, 672 (2008).

[20] R. Merino-Martinez, W. C. P. van der Velden, F. Avallone, and D. Ragni, *Acoustic measurements of a DU96–W–180 airfoil with flow–misaligned serrations at a high Reynolds number in a closed–section wind tunnel,* in 7th *International Meeting on Wind Turbine Noise, May 2 – 5 2017, Rotterdam, the Netherlands* (International Institute of Noise Control Engineering (I-INCE), 1A/B Westminster Chambers, 106 Lord Street, Southport PR8 1LF, United Kingdom, 2017).

[21] C. P. VanDercreek, R. Merino-Martinez, M. Snellen, and D. G. Simons, *Comparison of cavity geometries for a microphone array in a open–jet wind–tunnel experiment,* in 8th *Berlin Beamforming Conference, March 2 – 3 2020, Berlin, Germany* (GFaI, e.V., Berlin, 2020) BeBeC–2020–D7.

[22] T. Geyer, E. Sarradj, and C. Fritzsche, *Measurement of the noise generation at the trailing edge of porous airfoils,* Experiments in Fluids **48**, 291 (2010).

[23] A. Rubio Carpio, R. Merino-Martinez, F. Avallone, D. Ragni, M. Snellen, and S. van der Zwaag, *Experimental characterization of the turbulent boundary layer over a porous trailing edge for noise abatement,* Journal of Sound and Vibration **443**, 537 (2019).

[24] R. Merino-Martinez, M. P. J. Sanders, L. C. Caldas, F. Avallone, D. Ragni, L. D. de Santana, M. Snellen, and D. G. Simons, *Comparison between analog and digital microphone phased arrays for aeroacoustic measurements,* in 24th *AIAA/CEAS Aeroacoustics Conference, June 25 – 29 2018, Atlanta, Georgia, USA* (2018) AIAA paper 2018–2809.

[25] T. F. Brooks and W. M. Humphreys, *Extension of DAMAS Phased Array Processing for Spatial Coherence Determination (DAMAS–C),* in 12th *AIAA/CEAS Aeroacoustics Conference, May 8 – 10 2006, Cambridge, Massachusetts, USA* (2006) AIAA paper 2006–2654.

[26] P. Chiariotti, M. Martarelli, and P. Castellini, *Acoustic beamforming for noise source localization – Reviews, methodology and applications,* Mechanical Systems and Signal Processing **120**, 422 (2019).

[27] E. Sarradj, G. Herold, P. Sijtsma, R. Merino-Martinez, A. M. N. Malgoezar, M. Snellen, T. F. Geyer, C. J. Bahr, R. Porteous, D. J. Moreau, and C. J. Doolan, *A microphone array method benchmarking exercise using synthesized input data,* in 23rd *AIAA/CEAS Aeroacoustics Conference, June 5 – 9 2017, Denver, CO, USA* (2017) AIAA paper 2017–3719.

[28] G. Herold and E. Sarradj, *Performance analysis of microphone array methods,* Journal of Sound and Vibration **401**, 152 (2017).

[29] C. J. Bahr, W. M. Humphreys, D. Ernst, T. Ahlefeldt, C. Spehr, A. Pereira, Q. Leclère, C. Picard, R. Porteus, D. J. Moreau, J. Fischer, and C. J. Doolan, *A comparison of microphone phased array methods applied to the study of airframe noise in wind tunnel testing,* in 23rd *AIAA/CEAS Aeroacoustics Conference, June 5 – 9 2017, Denver, CO, USA* (2017) AIAA paper 2017–3718.

[30] R. Merino-Martinez, S. Luesutthiviboon, R. Zamponi, A. Rubio Carpio, D. Ragni, P. Sijtsma, M. Snellen, and C. Schram, *Assessment of the accuracy of microphone array methods for aeroacoustic measurements,* Journal of Sound and Vibration **470**, 1 (2020).

[31] F. R. Amaral, C. C. J. Pagani, and M. A. F. Medeiros, *Improvements in closed–section wind–tunnel beamforming experiments of acoustic sources distributed along a line,* Applied Acoustics **156**, 336 (2019).

[32] E. Sarradj, G. Herold, and S. Jekosch, *Array methods: Which one is the best?* in 7th *Berlin Beamforming Conference, March 5 – 6 2018, Berlin, Germany* (GFaI, e.V., Berlin, 2018) BeBeC–2018–S01.

[33] R. P. Dougherty, *Determining Spectra of Aeroacoustic Sources from Microphone Array Data,* in 25th *AIAA/CEAS Aeroacoustics Conference, May 20 – 23 2019, Delft, The Netherlands* (2019) AIAA paper 2019–2745.

[34] R. P. Dougherty, *Functional Beamforming,* in 5th *Berlin Beamforming Conference, February 19 – 20 2014, Berlin, Germany* (GFaI, e.V., Berlin, 2014) BeBeC–2014–01.

[35] R. P. Dougherty, *Functional Beamforming for Aeroacoustic Source Distributions,* in 20th *AIAA/CEAS Aeroacoustics Conference, June 16 – 20 2014, Atlanta GA, USA* (2014) AIAA paper 2014–3066.

[36] R. Merino-Martinez, M. Snellen, and D. G. Simons, *Functional beamforming applied to imaging of flyover noise on landing aircraft,* Journal of Aircraft **53**, 1830 (2016).

[37] R. Merino-Martinez, M. Snellen, and D. G. Simons, *Functional Beamforming Applied to Full Scale Landing Aircraft,* in 6th *Berlin Beamforming Conference, February 29 – March 1 2016, Berlin, Germany* (GFaI, e.V., Berlin, 2016) BeBeC–2016–D12.

[38] B. D. van Veen and K. M. Buckley, *Beamforming: A Versatile Approach to Spatial Filtering,* IEEE ASSP Magazine **5**, 4 (1988).

[39] P. Sijtsma, *CLEAN based on spatial source coherence,* International Journal of Aeroacoustics **6**, 357 (2007), SAGE Publications Ltd. London, United Kingdom.

[40] S. Luesutthiviboon, A. M. N. Malgoezar, R. Merino-Martinez, M. Snellen, P. Sijtsma, and D. G. Simons, *Enhanced HR–CLEAN–SC for resolving multiple closely spaced sound sources,* International Journal of Aeroacoustics **18**, 392 (2019).

[41] T. Suzuki, $L_1$ *generalized inverse beam–forming algorithm resolving coherent/incoherent, distributed and multipole sources,* Journal of Sound and Vibration **330**, 5835 (2011).

[42] E. Sarradj, C. Schulze, and A. Zeibig, *Identification of Noise Source Mechanisms using Orthogonal Beamforming,* in *Noise and Vibration: Emerging Methods* (2005).

[43] D. Blacodon and G. Élias, *Level Estimation of Extended Acoustic Sources Using a Parametric Method,* Journal of Aircraft **41**, 1360 (2004).

[44] A. M. N. Malgoezar, M. Snellen, R. Merino-Martinez, D. G. Simons, and P. Sijtsma, *On the use of global optimization methods for acoustic source mapping,* Journal of the Acoustical Society of America **141**, 453 (2017).

[45] D. H. Johnson and D. E. Dudgeon, *Array Signal Processing, Concepts and Techniques* (P T R Prentice Hall, Englewood Cliffs, 1993) ISBN: 978–0130485137.

[46] F. R. S. Lord Rayleigh, *XXXI. Investigations in Optics with special reference to the Spectroscope,* The London, Edinburgh and Dublin Philosophical Magazine and Journal of Science **8**, 261 (1879).

[47] E. Sarradj, *Three–Dimensional Acoustic Source Mapping with Different Beamforming Steering Vector Formulations,* Advances in Acoustics and Vibration **2012**, 1 (2012).

[48] T. F. Brooks and W. M. Humphreys, *Effect of Directional Array Size on the Measurement of Airframe Noise Components,* in 5th *AIAA/CEAS Aeroacoustics Conference. Bellevue, WA, USA* (1999) AIAA paper 1999–1958.

[49] R. Merino-Martinez, P. Sijtsma, and M. Snellen, *Inverse Integration Method for Distributed Sound Sources,* in 7th *Berlin Beamforming Conference, March 5 – 6 2018, Berlin, Germany* (GFaI, e.V., Berlin, 2018) BeBeC–2018–S07.

[50] R. Merino-Martinez, P. Sijtsma, A. Rubio Carpio, R. Zamponi, S. Luesutthiviboon, A. M. N. Malgoezar, M. Snellen, C. Schram, and D. G. Simons, *Integration methods for distributed sound sources,* International Journal of Aeroacoustics **18**, 444 (2019).

[51] R. Merino-Martinez, E. Neri, M. Snellen, J. Kennedy, D. G. Simons, and G. J. Bennett, *Comparing flyover noise measurements to full–scale nose landing gear wind–tunnel experiments for regional aircraft,* in 23rd *AIAA/CEAS Aeroacoustics Conference, June 5 – 9 2017, Denver, Colorado, USA* (2017) AIAA paper 2017–3006.

[52] R. Merino-Martinez, E. Neri, M. Snellen, J. Kennedy, D. G. Simons, and G. J. Bennett, *Analysis of nose landing gear noise comparing numerical computations, prediction models and flyover and wind–tunnel measurements,* in 24th *AIAA/CEAS Aeroacoustics Conference, June 25 – 29 2018, Atlanta, Georgia, USA* (2018) AIAA paper 2018–3299.

[53] R. P. Dougherty, *Mutual Incoherence of Broadband Duct Acoustic Modes,* in 22nd *AIAA/CEAS Aeroacoustics Conference, May 30 – June 1 2015, Lyon, France* (2016) AIAA paper 2016–3032.

[54] R. Merino-Martinez, L. Bertsch, M. Snellen, and D. G. Simons, *Analysis of landing gear noise during approach,* in 22nd *AIAA/CEAS Aeroacoustics Conference, May 30 – June 1 2016, Lyon, France* (2016) AIAA paper 2016–2769.

[55] R. Merino-Martinez, A. Vieira, M. Snellen, and D. G. Simons, *Sound quality metrics applied to aircraft components under operational conditions using a microphone array,* in 25th *AIAA/CEAS Aeroacoustics Conference, May 20 – 24 2019, Delft, The Netherlands* (2019) AIAA paper 2019–2513.

[56] E. Sarradj and C. Schulze, *Practical Application of Orthogonal Beamforming,* in *Proceedings Euronoise 2006, 30 May – 1 June, 2006, Tampere, Finland* (2006).

[57] E. Sarradj, *A fast signal subspace approach for the determination of absolute levels from phased microphone array measurements,* Journal of Sound and Vibration **329**, 1553 (2010).

[58] S. U. Pillai, *Array Signal Processing*, edited by C. S. Burrus (Springer, 1989) p. 313, ISBN: 978–3–540–96951–8.

[59] J. A. Högbom, *Aperture synthesis with a non–regular distribution of interferometer baselines,* Astronomy and Astrophysics Supplement Series **15**, 417 (1974).

[60] R. P. Dougherty and R. W. Stoker, *Sidelobe Suppresion for Phased Array Aeroacoustic Measurements,* in 4th *AIAA/CEAS Aeroacoustics Conference, June 2 – 4 1998, Toulouse, France* (1998) AIAA paper 1998–2242.

[61] P. Sijtsma, R. Merino-Martinez, A. M. N. Malgoezar, and M. Snellen, *High–Resolution CLEAN–SC: Theory and Experimental Validation,* International Journal of Aeroacoustics **16**, 274 (2017), SAGE Publications Ltd. London, United Kingdom.

[62] P. Sijtsma, R. Merino-Martinez, A. M. N. Malgoezar, and M. Snellen, *High–Resolution CLEAN–SC: Theory and Experimental Validation,* in 23rd *AIAA/CEAS Aeroacoustics Conference, June 5 – 9 2017, Denver, Colorado, USA* (2017) AIAA paper 2017–3841.

[63] S. Luesutthiviboon, A. Malgoezar, M. Snellen, P. Sijtsma, and D. G. Simons, *Improving Source Discrimination Performance by Using an Optimized Acoustic Array and Adaptive High–Resolution CLEAN–SC Beamforming,* in 7th *Berlin Beamforming Conference, March 5 – 6 2018, Berlin, Germany* (GFaI, e.V., Berlin, 2018) BeBeC–2018–D07.

[64] R. Merino-Martinez, E. Neri, M. Snellen, J. Kennedy, D. G. Simons, and G. J. Bennett, *Multi–approach study of nose landing gear noise,* Journal of Aircraft (2020), 10.2514/1.C035655.

[65] T. Yardibi, J. Li, P. Stoica, N. S. Zawodny, and L. N. Cattafesta III, *A covariance fitting approach for correlated acoustic source mapping,* Journal of the Acoustical Society of America **127**, 2920 (2010).

[66] G. Herold, E. Sarradj, and T. Geyer, *Covariance Matrix Fitting for Aeroacoustic Application,* in *Fortschritte der Akustik AIA - DAGA Merano* (2013) pp. 325–326.

[67] D. Blacodon, *Analysis of the Airframe Noise of an A320/A321 with a Parametric Method,* Journal of Aircraft **44**, 26 (2007).

[68] D. Blacodon, *Combustion–Noise Characterization of a Turbofan Engine with a Spectral Estimation Method,* Journal of Propulsion and Power 2009 **25**, 374 (2009).

[69] T. Suzuki and B. Day, *Comparative study on mode–identification algorithms using a phased–array system in a rectangular duct,* Journal of Sound and Vibration **347**, 27 (2015).

[70] R. Zamponi, N. van de Wyer, and C. Schram, *An Improved Regularization of the Generalized Inverse Beamforming Applied to a Benchmark Database,* in 7th *Berlin Beamforming Conference, March 5 – 6 2018, Berlin, Germany* (GFaI, e.V., Berlin, 2018) BeBeC–2018–D09.

[71] R. Zamponi, N. van de Wyer, and C. Schram, *Benchmark Assessment of an Improved Regularization Technique for Generalized Inverse Beamforming,* in 24th *AIAA/CEAS Aeroacoustics Conference, June 25 – 29 2018, Atlanta, Georgia, USA* (2018) AIAA paper 2018–4106.

[72] S. Jekosch, E. Sarradj, G. Herold, and T. F. Geyer, *Comparison of Different Solvers for General Inverse Beamforming Algorithms for High Resolution Aeroacoustic Source Characterization,* in 7th *Berlin Beamforming Conference, March 5 – 6 2018, Berlin, Germany* (GFaI, e.V., Berlin, 2018) BeBeC–2018–D08.

[73] C. L. Lawson and R. J. Hanson, *Solving least squares problems*, edited by S. for Industrial and A. Mathematics (Prentice–Hall, Inc., Englewood Cliffs, New Jersey, 1974) ISBN: 0–89871–356–0.

[74] E. Sarradj and G. Herold, *A Python framework for microphone array data processing,* Applied Acoustics **116**, 50 (2017).

[75] R. Merino-Martinez, A. Rubio Carpio, L. Tércio Lima Pereira, S. van Herk, F. Avallone, M. Kotsonis, and D. Ragni, *Aeroacoustic design and characterization of the 3D–printed, open–jet, anechoic wind tunnel of Delft University of Technology,* Applied Acoustics (2020), Under review.

[76] Flamex Basic – Acoustic Absorbing Foam, *https://www.merford.com/media/202626/flamex-basic.pdf,* Accessed in March 2017.

[77] G.R.A.S. Sound & Vibration – 40PH CCP Free–field array microphone, *http://www.gras.dk/products/special-microphone/array-microphones/product/178-40ph,* Accessed in March 2017.

[78] Visaton – Speaker K 50 SQ – 8 Ohm, *http://www.visaton.de/en/products/fullrange-systems/k-50-sq-8-ohm,* Accessed in March 2017.

[79] P. D. Welch, *The Use of Fast Fourier Transform for the Estimation of Power Spectra: A Method Based on Time Averaging Over Short, Modified Periodograms,* IEEE Transactions on Audio and Electroacoustics **AU–15**, 70 (1967).

[80] C. Arce León, R. Merino-Martinez, D. Ragni, F. Avallone, and M. Snellen, *Boundary layer characterization and acoustic measurements of flow–aligned trailing edge serrations,* Experiments in Fluids **57**, 1 (2016).

[81] C. Arce León, R. Merino-Martinez, D. Ragni, F. Avallone, F. Scarano, S. Pröbsting, M. Snellen, D. G. Simons, and J. Madsen, *Effect of trailing edge serration–flow misalignment on airfoil noise emission,* Journal of Sound and Vibration **405**, 19 (2017).

[82] C. Arce León, R. Merino-Martinez, S. Pröbsting, D. Ragni, and F. Avallone, *Acoustic Emissions of Semi–Permeable Trailing Edge Serrations,* Acoustics Australia **46**, 111 (2017).

[83] C. Arce León, R. Merino-Martinez, D. Ragni, S. Pröbsting, F. Avallone, A. Singh, and J. Madsen, *Trailing Edge Serrations – Effect of Their Flap Angle on Flow and Acoustics,* in 7th *International Meeting on Wind Turbine Noise, May 2 – 5 2017, Rotterdam, the Netherlands* (2017).

[84] J. D. J. Anderson, *Fundamentals of Aerodynamics*, Third ed. (McGraw–Hill Series in Aeronautical and Aerospace Engineering, 2001) ISBN: 0–07–237335–0.

[85] A. L. Braslow, R. M. Hicks, and R. V. Harris Jr., *Use of grit–type boundary–layer transition trips on wind–tunnel models*, Tech. Rep. NASA–TN–D–3579 (NASA Technical Note (D–3579), 1966).

[86] J. R. Underbrink, *Circularly symmetric, zero redundancy, planar array having broad frequency range applications,* (U.S. Patent number 6,205,224 B1. 2001).

[87] T. F. Brooks, D. S. Pope, and M. A. Marcolini, *Airfoil Self–Noise and Prediction*, Tech. Rep. NASA Reference Publication 1218 (NASA Reference Publication 1218, 1989).

[88] M. Tuinstra and P. Sijtsma, *Suppression of spurious noise sources in airfoil self–noise measurements,* in 21st *AIAA/CEAS Aeroacoustics Conference, June 22 – 26 2015, Dallas, TX, USA* (2015) AIAA paper 2015–2689.

[89] M. Drela, *XFOIL: an Analysis and Design System for Low Reynolds Number Airfoils*, Vol. 54 (Springer Berlin Heidelberg, 1989) part of Lecture Notes in Engineering book series (pp. 1–12). ISBN: 978–3–642–84010–4.

[90] S. Oerlemans, *Wind tunnel aeroacoustic tests of six airfoils for use on small wind turbines*, Tech. Rep. NREL/SR–500–35339 (National Renewable Energy Laboratory, 1617 Cole Boulevard, Golden, Colorado. 80401–3393. United States of America., 2004).

[91] S. Oerlemans and P. Migliore, *Aeroacoustic Wind Tunnel Tests of Wind Turbine Airfoils,* in 10th *AIAA/CEAS Aeroacoustics Conference, May 10 – 12, 2004, Manchester, United Kingdom* (2004) AIAA paper 2004–3042.